Indirect Detection via Spin-1/2 Nuclei in Solid State NMR Spectroscopy: Application to the Observation of Proximities between Protons and Quadrupolar Nuclei

Olivier Lafon,*,† Qiang Wang,†,‡,§ Bingwen Hu,† Filipe Vasconcelos,† Julien Trébosc,† Sylvain Cristol,† Feng Deng,‡ and Jean-Paul Amoureux†

Unité de Catalyse et de Chimie du Solide (UCCS), UMR CNRS 8181, École Nationale Supérieure de Chimie de Lille, Université de Lille 1, Bâtiment C7, B.P. 90108, 59652 Villeneuve d'Ascq Cedex, France, State Key Laboratory of Magnetic Resonance and Atomic and Molecular Physics, Wuhan Center for Magnetic Resonance, Wuhan Institute of Physics and Mathematics, Chinese Academy of Sciences, Wuhan 430071, People's Republic of China, and Graduate School of the Chinese Academy of Sciences, Beijing, People's Republic of China

Received: June 30, 2009; Revised Manuscript Received: August 28, 2009

We present a comprehensive comparison of through-space heteronuclear correlation techniques for solid state NMR, combining indirect detection and single-channel recoupling method. These techniques, named *D*-HMQC and *D*-HSQC, do not suffer from dipolar truncation and can be employed to correlate quadrupolar nuclei with spin-1/2 nuclei. The heteronuclear dipolar couplings are restored under magic-angle spinning by applying supercycled symmetry-based pulse sequences ($SR4_1^2$) or simultaneous frequency and amplitude modulation (SFAM). The average Hamiltonian theory (AHT) of these recoupling methods is developed. These results are applied to analyze the performances of *D*-HMQC and *D*-HSQC sequences. It is shown that, whatever the magnitude of spin interations, *D*-HMQC experiment offers larger efficiency and higher robustness than *D*-HSQC. Furthermore, the spectral resolution in both dimensions of proton detected two-dimensional *D*-HMQC and *D*-HSQC spectra can be enhanced by applying recently introduced symmetry-based homonuclear dipolar decoupling schemes that cause a *z*-rotation of the spins. This is demonstrated by $^1H-^{13}C$ and $^1H-^{23}Na$ correlation experiments on L-histidine and NaH_2PO_4, respectively. The two-dimensional heteronuclear $^1H-^{23}Na$ correlation spectrum yields the assignment of ^{23}Na resonances of NaH_2PO_4. This assignment is corroborated by first-principles calculations.

1. Introduction

Two-dimensional (2D) heteronuclear correlation (HETCOR) nuclear magnetic resonance (NMR) spectroscopy is a valuable tool for the characterization and structural investigation of solid state compounds under magic-angle spinning (MAS). First, these methods facilitate spectral assignment owing to the improved resolution and information on the *J*-couplings or dipolar couplings. Second, the HETCOR experiments can also be employed to observe indirectly an isotope via a spy nucleus. In particular, such a strategy has been applied for the observation of integer (^{14}N) or half-integer (^{27}Al, ^{23}Na, ...) quadrupolar nuclei, $I > 1/2$, via nearby spin-1/2 spy nuclei.[1−11] Third, the HETCOR experiments allow probing the local environment of atoms, since the *J*-couplings and dipolar couplings reveal the through-bond connectivities and the through-space proximities, respectively. Hence the HETCOR methods using coherence transfers via the dipolar couplings (*D*-HETCOR) or via the *J*-couplings (*J*-HETCOR) are complementary. The *J*-HETCOR techniques help in identifying the molecular entities in solid state compounds, while the *D*-HETCOR methods can be used to establish their three-dimensional structures and to reveal the noncovalent intra- and intermolecular interactions (ionic and hydrogen bonds, π-stacking, ...).

A variety of *J*-HETCOR and *D*-HETCOR pulse sequences have been proposed so far. Figure 1 summarizes their main properties. The sequences are classified according to the mode of detection, direct or indirect, and the order of coherences during the t_1 evolution period. The *J*-HETCOR methods include the directly detected *J*-INEPT experiment[12,13] as well as the indirectly detected *J*-HSQC and *J*-HMQC schemes.[8,14−19] However, *D*-HETCOR experiments are generally more efficient than the *J*-HETCOR.[5−7,10,11] This arises from the large size of dipolar couplings, allowing the use of short recoupling times in *D*-HETCOR experiments. The *D*-HETCOR methods using direct detection comprise cross-polarization (CP)[20,21] or *D*-INEPT sequences.[22,23] The *D*-INEPT methods derives from the *J*-INEPT experiment, but heteronuclear dipolar recoupling techniques are applied during the defocusing and refocusing delays in order to restore the dipolar couplings under MAS. TEDOR sequence is an example of the *D*-INEPT method, where the employed dipolar recoupling method is REDOR.[24,25] However, indirect detection can enhance the sensitivity of *D*-HETCOR experiments, depending on the gyromagnetic ratios, γ, longitudinal relaxation times, T_1, and spectral line widths of the correlated nuclei.[26] In particular, inverse proton detection of ^{13}C and ^{15}N nuclei can become advantageous at high MAS frequency ($\nu_r \geq 30$ kHz).[26−31] The *D*-HETCOR methods employing indirect detection include consecutive CP transfers (denoted double CP),[26−31] heteronuclear multiquantum spectroscopy by dual symmetry-based pulse sequences,[32] and the *D*-HSQC and *D*-HMQC techniques.[5,6,23,33−35] The *D*-HSQC and *D*-HMQC experiments are adapted from *J*-HSQC and *J*-HMQC schemes, which are employed to characterize the chemical bonds in liquids and solids.[8,14−19]

In CP and dual symmetry-based pulse sequences, resonant radio frequency (rf) irradiation is applied to both spin species

---

[†] Université de Lille 1.

[‡] Chinese Academy of Sciences.

[§] Graduate School of the Chinese Academy of Sciences.

10.1021/jp906099k CCC: $40.75

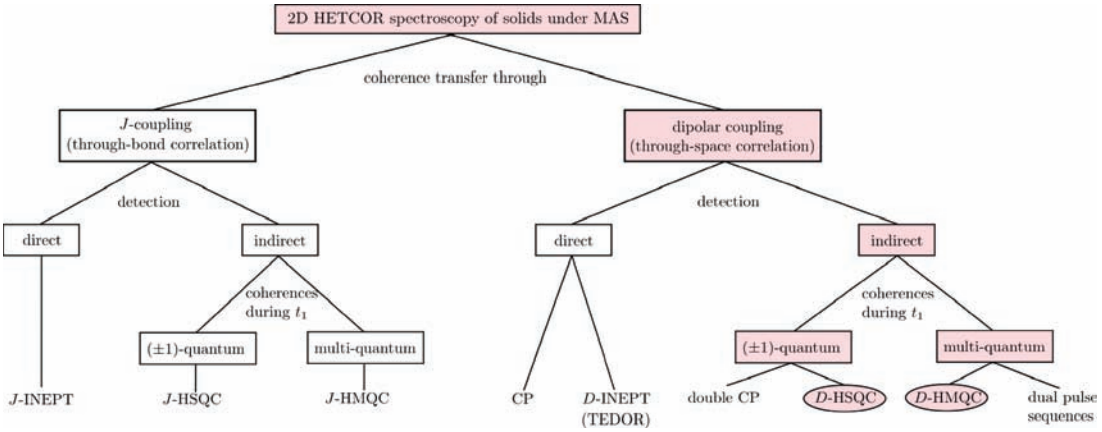

Figure 1. Schematic classification of 2D heteronuclear correlation NMR experiments, which can be employed to characterize solid state compounds under MAS condition. The paths corresponding to *D*-HMQC and *D*-HSQC sequences are highlighted.

I and *S* to achieve heteronuclear dipolar recoupling. However, the recoupled heteronuclear dipolar interactions do not commute for different pairs and these techniques suffer from dipolar truncation.[36,37] Hence the short-range dipolar couplings average the long-range ones, with the consequence that the long-range through-space proximities cannot be observed. Furthermore, CP and dual pulse sequences involving quadrupolar nuclei is a complicated process because of the difficulty to selectively rotate the central-transition polarization.[11,38] For these nuclei, multiple-pulse CP sequences outperform the continuous-wave CP transfer.[39] However, CP involving quadrupolar nuclei yields generally low sensitivity and is not robust to resonance offset and rf inhomogeneity.[40]

D-HSQC and *D*-HMQC methods alleviate these shortcomings. First, the dipolar recoupling sequences in *D*-HSQC and *D*-HMQC accomplish a *longitudinal two-spin-order* (I_zS_z) recoupling of the dipolar interactions.[32,41,42] This recoupled Hamiltonian commutes across different spin pairs and therefore does not suffer from dipolar truncation, allowing the observation of both short- and long-range correlations between heteronuclear spins. Second, longitudinal two-spin-order recoupling can be generated by the application of rf fields to only one of the spin species, which can be either the undetected spins (*I*) or the detected ones (*S*). This is clearly an advantage when using *D*-HMQC or *D*-HSQC experiments to correlate quadrupolar and spin-1/2 nuclei, since the number of pulses sent on the quadrupolar channel can be minimized by applying the heteronuclear recoupling sequences to the spin-1/2 nucleus.

The difference between *D*-HMQC and *D*-HSQC techniques lies in the order of coherences evolving during the t_1 period and in the number of rf pulses. Multiple-quantum (MQ) and single-quantum (1Q) coherences are selected during t_1 by *D*-HMQC and *D*-HSQC, respectively. Thus, in *D*-HSQC, the F_1 spectral dimension is immune to both homogeneous and inhomogeous decays of the coherence of the spy nucleus during the t_1 period. Consequently, the 1Q scheme can provide higher resolution than the MQ scheme.[8,9,17] This possible gain in resolution comes at the expense of a larger number of rf pulses, which may decrease the sensitivity especially in the case of quadrupolar nuclei. Nevertheless, variants of HSQC with limited number of pulses have been proposed in solids.[8,9] They are especially suitable for *D*-HETCOR involving quadrupolar nuclei, since they allow decreasing the number of pulses applied to the quadrupolar spins. The performances of *D*-HMQC and *D*-HSQC also depend on the choice of the heteronuclear recoupling sequence. Different longitudinal two-spin-order recoupling methods with single channel irradiation can be employed, including REDOR,[24,25] rotary resonance recoupling (R^3),[43−46] simultaneous frequency and amplitude modulation (SFAM),[35,47,48] and symmetry-based sequences, e.g., R12_3^5, R20_5^9, and SR4_1^2.[7,32,41,49] We have recently demonstrated that SR4_1^2 and SFAM sequences provide higher efficiency and robustness to rf inhomogeneity or maladjustment than the other recoupling schemes.[35] Nevertheless, the robustness to resonance offset and the effect of the position of the recoupling sequence—in the undetected or detected channels—have not been investigated so far.

In this contribution, we will compare the performances of *D*-HMQC and *D*-HSQC experiments in solids, with a view to employing these techniques in order to correlate a quadrupolar nucleus with a spin-1/2 nucleus. Hence, only *D*-HSQC sequences with restricted numbers of pulses will be considered. Furthermore, only SR4_1^2 and SFAM sequences will be employed as heteronuclear recoupling methods. In particular, we will analyze in detail how the position of the heteronuclear recoupling sequence affects the efficiency and the robustness of *D*-HMQC and *D*-HSQC. We will also demonstrate that, in the case of inverse proton detection, the spectral resolution in both dimensions F_1 and F_2 can be improved by applying the recently introduced C8_1^4(half-cos) homonuclear decoupling scheme.[10,50,51] In the following, the indirectly detected spin is denoted *I* and the detected spy spin *S*. We refer to the *D*-HMQC and *D*-HSQC experiments involving $S \rightarrow I \rightarrow S$ polarization transfers as "$I-S$".

This article is organized as follows. Section 2 will introduce the zero-order average Hamiltonian (AH) theory of the *D*-HMQC and *D*-HSQC pulse sequences.[52,53] The analytical predictions will be tested by numerical simulations. In section 3, experimental results will be presented. The dependence of *D*-HMQC and *D*-HSQC sensitivity with offset will be illustrated by experiments on glycine. The properties of *D*-HMQC and *D*-HSQC methods will be also compared in 2D ^{13}C−^{1}H and ^{23}Na−^{1}H correlation experiments on L-histidine and NaH_2PO_4. We show how *D*-HMQC experiment incorporating the C8_1^4(half-cos) decoupling scheme permits the assignment of ^{23}Na resonances of NaH_2PO_4. This assignment will be supported by periodic density functional theory (DFT) calculations.[54]

2. Theory

2.1. *D*-HMQC and *D*-HSQC Pulse Sequences.

The basic pulse sequences for *D*-HMQC and *D*-HSQC experiments are shown in Figure 2a and 2b, respectively. The indirectly detected

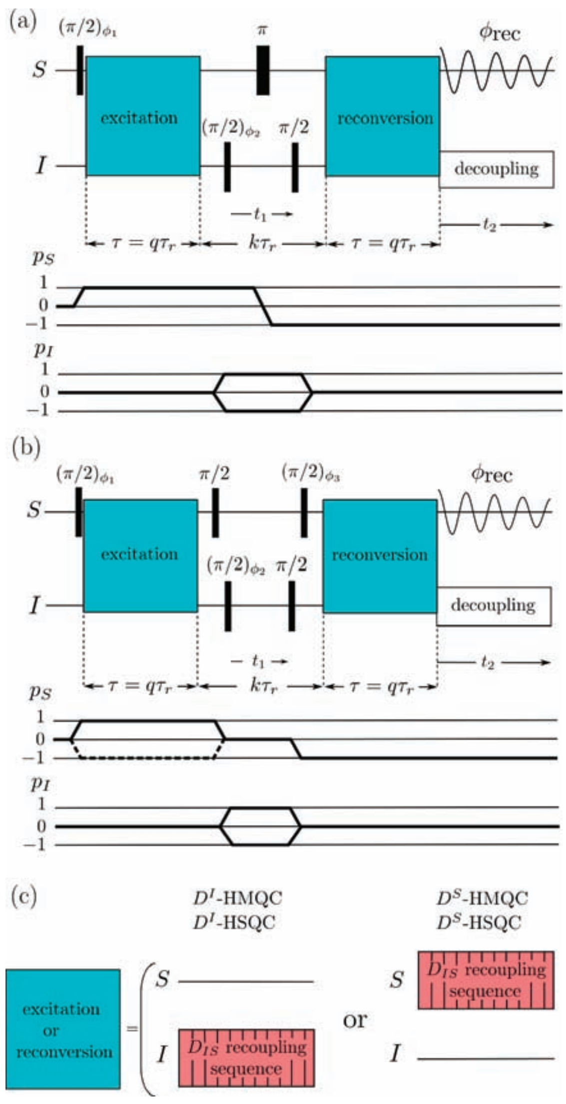

Figure 2. Pulse sequences and coherence transfer pathways for (a) *D*-HMQC and (b) *D*-HSQC experiments. In (b), two coherence transfer pathways are shown during excitation period. *D*-HSQC(±1) experiment allows both pathways, while *D*-HSQC(+1) variant only selects the one shown as a continuous line. Coherence pathways were selected by the following phase cyclings: (i) for *D*-HMQC, $\phi_1 = \pi/2(\text{floor})(m_c/2)$, $\phi_2 = \pi m_c$, and $\phi_{\text{rec}} = -\phi_1 - \phi_2$, where m_c denote the phase cycle counter; (ii) for *D*-HSQC(±1), $\phi_1 = \pi(\text{floor})(m_c/2)$, $\phi_2 = \pi m_c$, $\phi_3 = \pi/2(\text{floor})(m_c/4)$, and $\phi_{\text{rec}} = -\phi_1 - \phi_2 + \phi_3$; (iii) for *D*-HSQC(+1), $\phi_1 = \pi/2(\text{floor})(m_c/2)$, $\phi_2 = \pi m_c$, $\phi_3 = \pi(\text{floor})(m_c/8)$, and $\phi_{\text{rec}} = -\phi_1 - \phi_2 + \phi_3$. Quadrature detection in indirect dimension was achieved using the States-TPPI procedure[56] by incrementing the phase ϕ_2. (c) During τ intervals, heteronuclear dipolar recoupling sequences are used to recover the heteronuclear dipolar interaction. These sequences can be applied to either the undetected (I) or detected (S) spins.

spin is denoted I and the detected spy spin S. These experiments exploit IS dipolar couplings, D_{IS}, for the transfers of coherence from spin S to I and back. The heteronuclear D_{IS}-couplings are restored under MAS by applying heteronuclear dipolar recoupling techniques during the excitation and reconversion delays, τ. Thus, during the first τ, the S-spin magnetization for a pair of coupled IS spins evolves from in-phase (S_x) into antiphase ($2I_zS_y$) coherence with respect to I. In the *D*-HMQC experiment [see Figure 2a], this antiphase S-spin 1Q coherence is converted into a heteronuclear MQ coherence ($2I_xS_y$) by the $(\pi/2)_{\phi_2}$ pulse on the I channel, while in the *D*-HSQC experiment [see Figure 2b] two simultaneous $\pi/2$ pulses applied on both channels transform this antiphase S-spin 1Q coherence into an antiphase heteronuclear 1Q I-spin coherence ($2I_xS_z$). The isotropic chemical shift, δ^I_{iso}, I nucleus is then encoded by allowing these MQ or 1Q coherences to evolve during the indirect evolution time, t_1. For an I-spin experiencing quadrupolar interaction, the peak resonance frequency along the indirect dimension is shifted from the δ^I_{iso} value by the quadrupolar isotropic shift, ν^I_{QIS}.[55] In principle, an additional π pulse on the S channel can be inserted in the middle of the t_1 period of the *D*-HSQC experiment in order to refocus the isotropic heteronuclear *J*-couplings, J_{IS}, between S- and I-spins. However, this π S-pulse is not always essential in solids, since the J_{IS}-couplings are generally much smaller than the line widths in F_1 dimension.[8,9] This prevails especially for the indirect observation of quadrupolar nuclei.

At the end of t_1, the MQ and 1Q coherences are converted back into antiphase S-spin coherences by the $\pi/2$ pulses, and these coherences evolve during the second τ to become observable transverse S-spin magnetization. A 2D Fourier transform of the time domain signal provides isotropic shift correlations between pairs of I and S nuclei.

For half-integer spin quadrupolar nuclei, only correlations involving the central transition (CT) $-1/2 \leftrightarrow 1/2$ are observed in 2D *D*-HMQC and *D*-HSQC spectra. The central transition is not broadened by the first-order quadruprolar interaction. The CT polarizations are excited and rotated by using CT selective rf pulses. When the S spin is half-integer and experiences quadrupolar interaction, the anisotropic second-order terms of quadrupolar interaction must be averaged out by combining MAS and rotor synchronization of the delay between the centers of the first and the second S-pulses as well as the delay between the center of the last S-pulse and the start of the acquisition period, t_2, in both HMQC and HSQC sequences.[23] Integer spin quadrupolar nuclei, such as ^{14}N, are generally indirectly detected. In that case, the t_1 period, defined as the interval between the centers of the two pulses on the I channel, must be an integer multiple of the rotor period for the complete averaging of the first-order quadrupolar interaction.[4]

The quadrupolar interaction also affects the *D*-HMQC and *D*-HSQC efficiencies since it complexifies the spin dynamics during the rf pulses. However, for the indirect detection of quadrupolar nuclei via protons, the quadrupolar interaction does not modify the relative efficiency of *D*-HMQC and *D*-HSQC experiments, since the I-spins are subjected to the same rf pulses in both sequences [see Figure 2a,b].

2.2. Heteronuclear Dipolar Recoupling. In this work, we applied either SR4_1^2 or SFAM recoupling techniques during the τ delays in order to restore the dipolar D_{IS}-couplings. These rotor-synchronized sequences have common properties. First, they accomplish heteronuclear dipolar recoupling by irradiating only one of the isotopes, either I- or S-spins. Thus, for correlation between quadrupolar and spin-1/2 nuclei, the SR4_1^2 or SFAM sequences can be applied only to the spin-1/2 nuclei. This allows avoiding interferences between quadrupolar interaction and rf field. Second, these recoupling sequences are not γ-encoded[42,57] and hence the interval between the excitation and reconversion delays must be an integer multiple of the rotor period, $k\tau_r$, as shown in Figure 2a,b. Third, these recoupling sequences applied on a single rf channel recouple the chemical shift anisotropy (CSA) interactions of the irradiated spins at the same time as the heteronuclear D_{IS} interactions, since these terms evolve identically under sample rotation and rf irradiation of a single spin. However, the recoupled terms of the CSA and the heteronuclear D_{IS}-couplings commute. Therefore, the evolution of spin coherences due to the D_{IS}-couplings is not affected by the CSA of irradiated spins. Additional features of these sequences are summarized below.

2.2.1. SR4$_1^2$ Recoupling. The SR4$_1^2$ pulse sequence is constructed from the symmetry-based R4$_1^2$ sequence employing a single 180_0 pulse as a basic element.[49] Here β_ϕ indicates a rectangular, resonant rf pulse with flip angle β and phase ϕ (both in degrees). The basic R4$_1^2$ sequence, which consists of four 180° pulses, spans one rotor period and requires the rf field strength to be twice the spinning frequency. A nested supercycle is constructed by first forming a phase inversion sequence R4$_1^2$R4$_1^{-2}$ and subsequently applying a three-step MQ-phase cycling. The SR4$_1^2$ pulse sequence can be denoted (R4$_1^2$R4$_1^{-2}$)3^1.

Consider the case where the SR4$_1^2$ sequence is applied to the I-spins. The symmetry-based selection rules entail that the zero-order AH, $\bar{\mathscr{H}}^{(0)}$, contains D_{IS}-couplings, CSA of the I-spin, CSA$_I$, chemical and quadrupolar isotropic shifts of the S-spin, δ_{iso}^S and ν_{QIS}^S, and homonuclear isotropic J-couplings, J_{II} and J_{SS}, while all the terms of the homonuclear dipolar couplings between I-spins, D_{II}, δ_{iso}^I shifts, and J_{IS}-couplings between I- and S-spins are suppressed to zero order. Thus the $\bar{\mathscr{H}}^{(0)}$ Hamiltonian of a heteronuclear I_2S spin system during R4$_1^2$R4$_1^{-2}$ or SR4$_1^2$ irradiation can be written

$$\bar{\mathscr{H}}^{(0)} = \left(\sum_{j=1,2} \omega_{D,jS} I_{jz} S_z + \omega_{\mathrm{CSA},j} I_{jz}\right) + 2\pi J_{II} I_1 I_2 + \Omega_S^0 S_z + \bar{\mathscr{H}}_{\mathrm{Q},S}^{(2)} \quad (1)$$

The $\bar{\mathscr{H}}^{(0)}$ Hamiltonian results from averaging over an even number of rotor periods. In eq 1, $\omega_{D,jS}$ with $j = 1, 2$ is the magnitude of the recoupled D_{IS}-coupling between I_j- and S-spins, $\omega_{\mathrm{CSA},j}$ is the magnitude of the recoupled CSA of I_j-spin, J_{II} is the homonuclear isotropic J-coupling between I-spins, and Ω_S^0 is the resonance offset frequency (isotropic chemical shift) of S-spin. $\bar{\mathscr{H}}_{\mathrm{Q},S}^{(2)}$ is the Hamiltonian of the second-order quadrupolar interaction averaged by MAS.[55] This term is null in the case of spin-1/2 nucleus, whereas it produces ν_{QIS}^S shift for quadrupolar nucleus. The CSA$_S$ and the first-order quadrupolar interaction of S-spin are absent in eq 1 since they are averaged out by MAS over an integer number of rotor period. The magnitude of homonuclear J_{II}-coupling is not scaled by SR4$_1^2$ irradiation since this interaction is left unchanged by sample rotation and rf irradiation of both I_1- and I_2-spins. When the SR4$_1^2$ sequence is applied to the S-spins of a IS_2 spin system, $\bar{\mathscr{H}}^{(0)}$ becomes

$$\bar{\mathscr{H}}^{(0)} = \left(\sum_{j=1,2} \omega_{D,Ij} I_z S_{jz} + \omega_{\mathrm{CSA},j} S_{jz}\right) + 2\pi J_{SS} S_1 S_2 + \Omega_I^0 I_z + \bar{\mathscr{H}}_{\mathrm{Q},I}^{(2)} \quad (2)$$

Compared to eq 2, the I and S symbols are simply interchanged. The frequencies ω_Λ with $\Lambda = D, jS$; D, Ij; or CSA, j in eqs 1 and 2 are given by[49]

$$\omega_\Lambda = \kappa \,\mathrm{Re}\{[A_{22}^\Lambda]^R \exp[-2\imath(\alpha_{RL}^0 - \omega_r t_0)]\} \quad (3)$$

where the scaling factor is $\kappa = 1/(6^{1/2})$ for SR4$_1^2$ sequence. t_0 refers to the starting time point of the pulse sequence and α_{RL}^0 denotes the initial rotor position. $[A_{22}^\Lambda]^R$ is the space component $m = 2$ of interaction Λ with space rank $l = 2$, expressed in the rotor-fixed frame. The space component of D_{IS}-coupling is given by

$$[A_{22}^{D,jS}]^R = \frac{3}{2} b_{jS} \exp(-2\imath\gamma_{PR}^{D,jS}) \sin^2(\beta_{PR}^{D,jS}) \quad (4)$$

where $\{\alpha_{PR}^{D,jS}, \beta_{PR}^{D,jS}, \gamma_{PR}^{D,jS}\}$ are the Euler angles relating the internuclear vector $\mathbf{r}_{jS}$ to the MAS rotor-fixed frame. The dipolar coupling constant b_{jS} is related to the internuclear distance r_{jS} and the gyromagnetic ratios γ_S and γ_I by $b_{jS} = -(\mu_0/4\pi)\gamma_S\gamma_I\hbar/(r_{jS}{}^3)$ in SI units. The space component of CSA is equal to

$$[A_{22}^{\mathrm{CSA},j}]^R = -\frac{6^{1/2}}{4}\gamma_I B^0 \delta_{\mathrm{aniso}}^j \exp(-2\imath\gamma_{PR}^{\mathrm{CSA},j})\Big[\sin^2(\beta_{PR}^{\mathrm{CSA},j}) - \frac{\eta_{\mathrm{CS}}^j}{3}\{[1 + \cos^2(\beta_{PR}^{\mathrm{CSA},j})]\cos(2\alpha_{PR}^{\mathrm{CSA},j}) - 2\imath\cos(\beta_{PR}^{\mathrm{CSA},j})\sin(2\alpha_{PR}^{\mathrm{CSA},j})\}\Big] \quad (5)$$

where $\{\alpha_{PR}^{\mathrm{CSA},j}, \beta_{PR}^{\mathrm{CSA},j}, \gamma_{PR}^{\mathrm{CSA},j}\}$ are the Euler angles describing the orientation of the principal axis frame of the CSA $_j$ tensor in the rotor-fixed frame. B^0 is the magnitude of the external static magnetic field, $\delta_{\mathrm{aniso}}^j = \delta_{\mathrm{zz}}^j - \delta_{\mathrm{iso}}^j$ is the anisotropic chemical deshielding constant, and $\eta_{\mathrm{CS}}^j = (\delta_{\mathrm{yy}}^j - \delta_{\mathrm{xx}}^j)/\delta_{\mathrm{aniso}}^j$ is the asymmetry parameter.[58] The isotropic chemical shift is given by $\delta_{\mathrm{iso}}^j = (\delta_{\mathrm{xx}}^j + \delta_{\mathrm{yy}}^j + \delta_{\mathrm{zz}}^j)/3$, and δ_{xx}^j, δ_{yy}^j, and δ_{zz}^j denote the principal values of the chemical shift tensor, labeled such that $|\delta_{\mathrm{zz}}^j - \delta_{\mathrm{iso}}^j| \geq |\delta_{\mathrm{xx}}^j - \delta_{\mathrm{iso}}^j| \geq |\delta_{\mathrm{yy}}^j - \delta_{\mathrm{iso}}^j|$.

2.2.2. SFAM-N Recoupling. The SFAM-N sequences are rotor-synchronized single-channel irradiations employing simultaneous cosinusoidal and sinusoidal time modulations of the carrier frequency and rf field amplitude.[35,47] The angular modulation frequency is N times the angular spinning frequency, ω_{r}. In the following, we will consider the case where the SFAM-N sequence is applied to the I-spins. When it is applied to the S channel, the I and S symbols must be interchanged. During a SFAM-N scheme, the instantaneous amplitude of the rf field experienced by I-spins is given by

$$\omega_{\mathrm{nut}I}(t) = \omega_{\mathrm{nut}I}^{\max} \sin[N\omega_{\mathrm{r}}(t - t_0)] \quad (6)$$

where $\omega_{\mathrm{nut}I}^{\max}$ is the peak amplitude of the rf field. In a suitably chosen rotating frame, the instantaneous modulation of the carrier frequency is

$$\Delta\omega_{\mathrm{ref}I}(t) = \Delta\omega_{\mathrm{ref}I}^{\max} \cos[N\omega_{\mathrm{r}}(t - t_0)] \quad (7)$$

where $\Delta\omega_{\mathrm{ref}I}^{\max}$ is the peak amplitude of the modulation.

In this rotating frame, the SFAM-N sequences produce an effective field of magnitude

$$\omega_{\mathrm{eff}I}(t) = \left[\omega_{\mathrm{nut}I}(t)^2 + \Delta\omega_{\mathrm{ref}I}(t)^2\right]^{1/2} \quad (8)$$

This effective field revolves around the y-axis with an apparent frequency[47]

$$\omega_{\mathrm{app}I}(t) = \frac{\omega_{\mathrm{nut}I}^{\max}\Delta\omega_{\mathrm{ref}I}^{\max} N\omega_{\mathrm{r}}}{\omega_{\mathrm{eff}I}^2(t)} \quad (9)$$

The $\bar{\mathscr{H}}^{(0)}$ Hamiltonian depends on the relative values of ω_r, ω_{nutI}^{max}, and $\Delta\omega_{refI}^{max}$. An analytical expression of $\bar{\mathscr{H}}^{(0)}$ can only be derived in some limit cases, such as $\omega_{effI}(t) \gg \omega_{appI}(t)$ or $\omega_{nutI}^{max} \gg \Delta\omega_{refI}^{max}$, which are discussed below.

SFAM-N Sequences When $\omega_{effI}(t) \gg \omega_{appI}(t)$. The fulfillment of this condition requires frequencies ω_{nutI}^{max} and $\Delta\omega_{refI}^{max}$ to be both much larger than $N\omega_r$. This case was treated by Fu et al.[47] However, the D_{II}-couplings were not considered explicitly. Here we specify the analytical expression of the different terms in $\bar{\mathscr{H}}^{(0)}$ when the SFAM-N sequences are applied to spin-1/2 nuclei.

If $\omega_{effI}(t) \gg \omega_{appI}(t)$, the SFAM-1 and SFAM-2 irradiations achieve longitudinal two-spin-order recoupling of the D_{IS}-couplings while suppressing the δ_{iso}^I shifts of the irradiated spin and the J_{IS}-couplings. The J_{II}-couplings are not affected by the SFAM-N irradiations.

Like the $SR4_1^2$ sequence, the SFAM-2 irradiation also removes the D_{II}-couplings when $\omega_{effI}(t) \gg \omega_{appI}(t)$. This result is demonstrated in the Supporting Information, section 1.2. Therefore, during SFAM-2 irradiation, the $\bar{\mathscr{H}}^{(0)}$ Hamiltonian of an I_2S spin system is given by eq 1. Furthermore, as SFAM-2 and $SR4_1^2$ sequences both recouple the space component $m = 2$ of D_{IS}-couplings and CSA_I interactions, the ω_Λ frequency with $\Lambda = D, jS$ or CSA, j is given by eq 3 for the SFAM-2 scheme. Only the scaling factor κ differs between the two recoupling methods. For the SFAM-2 scheme, the D_{IS}-coupling and CSA scaling factor is equal to $\kappa = C_1/6^{1/2}$, where C_1 is the first coefficient in the Fourier cosine series expansion of $\cos\theta(t) = \Delta\omega_{refI}(t)/\omega_{nutI}(t)$, and $\theta(t)$ is the tilt angle between the B^0-axis and the effective rf field of magnitude $\omega_{effI}(t)$.[46] The C_1 coefficient is a function of the parameter $\xi = \omega_{nutI}^{max}/\Delta\omega_{refI}^{max}$. For $\omega_{nutI}^{max} = \Delta\omega_{refI}^{max} \gg N\omega_r$, we have $C_1 = 1$ and SFAM-2 and $SR4_1^2$ sequences achieve identical heteronuclear dipolar recoupling at zero order.

Contrary to SFAM-2 and $SR4_1^2$, the SFAM-1 irradiation does not remove the D_{II}-couplings. Therefore, when applied to the I_2S spin system, the SFAM-1 scheme yields the zero-order AH

$$\bar{\mathscr{H}}^{(0)} = \left(\sum_{j=1,2}\omega_{D,jS}I_{jz}S_z + \omega_{CSA,j}I_{jz}\right) + \omega_{D,II}\left[2I_{1z}I_{2z} - \frac{1}{2}(I_1^+I_2^- + I_1^-I_2^+)\right] + 2\pi J_{II}I_1I_2 + \Omega_S^0S_z + \bar{\mathscr{H}}_{Q,S}^{(2)} \quad (10)$$

In eq 10, the notations are the same as in eq 1 and $\omega_{D,II}$ is the magnitude of the recoupled homonuclear dipolar coupling between I-spins. The SFAM-1 scheme reintroduces the space component $m = 1$ of D_{IS}-couplings and CSA_I. Thus the frequencies ω_Λ with $\Lambda = D, jS$ or CSA,j in eq 10 are equal to

$$\omega_\Lambda = \kappa\,\mathrm{Re}\{[A_{21}^\Lambda]^R\exp[-\iota(\alpha_{RL}^0 - \omega_r t_0)]\} \quad (11)$$

using the same notation as in eq 3. The scaling factor of SFAM-1 scheme is equal to $\kappa = -C_1/3^{1/2}$. Its magnitude is multiplied by $2^{1/2}$ compared to that of SFAM-2 in the same conditions. Therefore, SFAM-1 requires a shorter recoupling time than SFAM-2 and $SR4_1^2$.[35] $[A_{21}^\Lambda]^R$ is the space component $m = 1$ of interaction Λ with space rank $l = 2$, expressed in the rotor-fixed frame. For the D_{IS}-coupling, the space component is given by

$$[A_{21}^{D,jS}]^R = \frac{3}{2}b_{jS}\exp(-\iota\gamma_{PR}^{D,jS})\sin(2\beta_{PR}^{D,jS}) \quad (12)$$

using the same notation as in eq 4. The space component for the CSA is equal to

$$[A_{21}^{CSA,j}]^R = -\frac{6^{1/2}}{2}\gamma_I B^0\delta_{aniso}^j\exp(-\iota\gamma_{PR}^{CSA,j})\sin(\beta_{PR}^{CSA,j})\left\{\cos(\beta_{PR}^{CSA,j}) + \frac{\eta_{CS}^j}{3}[\cos(\beta_{PR}^{CSA,j})\cos(2\alpha_{PR}^{CSA,j}) - \iota\sin(2\alpha_{PR}^{CSA,j})]\right\} \quad (13)$$

using the same notation as in eq 5.

Furthermore, the SFAM-1 scheme also recouples the space component $m = 2$ of D_{II}-coupling. Hence, the frequency $\omega_{D,II}$ in eq 10 is given by eq 3 with $\Lambda = D, II$. The component $[A_{22}^{D,II}]^R$ has an analytical expression identical to that of $[A_{22}^{D,jS}]^R$ [see eq 4]. For the SFAM-1 scheme, the scaling factor of D_{II}-coupling is $\kappa = C_1^{D,II}/6^{1/2}$, where $C_1^{D,II}$ is the first coefficient in the Fourier cosine series expansion of the function $\{3\cos^2[\theta(t)] - 1\}/2$ of the tilt angle. The demonstration is given in the Supporting Information, section 1.2. For $\omega_{nutI}^{max} = \Delta\omega_{refI}^{max} \gg N\omega_r$, we have $C_1^{D,II} = 0.75$ and $\kappa = 0.75/6^{1/2} = 0.31$.

The above derivation shows that an analytical expression for $\bar{\mathscr{H}}^{(0)}$ during SFAM-N irradiations can be obtained when the magnitude of the effective field is much larger than its apparent revolving frequency around the y-axis. This approximation $\omega_{effI}(t) \gg \omega_{appI}(t)$ is only valid for large modulations of both rf field amplitude and carrier frequency ($\omega_{nutI}^{max} \gg N\omega_r$ and $\Delta\omega_{refI}^{max} \gg N\omega_r$). These large modulations can produce significant rf pulse transients, which can affect the recoupling performances.[59] However, the fulfillment of the condition $\omega_{effI}(t) \gg \omega_{appI}(t)$ is not essential to achieve heteronuclear dipolar recoupling with SFAM-N methods and experimentally carrier frequency modulations smaller than $N\omega_r$ were employed.[35,47] We show below that an analytical expression of $\bar{\mathscr{H}}^{(0)}$ can be derived in the regime $\Delta\omega_{refI}^{max} < N\omega_r$, provided the modulation of the rf field amplitude is larger than that of the carrier frequency ($\omega_{nutI}^{max} \gg \Delta\omega_{refI}^{max}$). As this regime is mainly advantageous for SFAM-2, we will only consider the case of SFAM-2 in the following.

SFAM-2 Sequence When $\omega_{nutI}^{max} \gg \Delta\omega_{refI}^{max}$. When this condition is satisfied during SFAM-2 irradiation, the recoupled D_{IS}-couplings are scaled by the first-order Bessel function of the first kind, $J_1(\psi)$, where $\psi = \omega_{nutI}^{max}/(2\omega_r)$. On the contrary, the magnitude of the recoupled D_{II}-couplings depends on $J_1(2\psi)$. The demonstration is given in the Supporting Information, section 1.3. Plots of $J_1(\psi)$ and $J_1(2\psi)$ versus ψ are shown in Figure 3. As seen in the figure, the condition $\omega_{nutI}^{max} = 3.82\omega_r$ corresponds to the lowest rf field, allowing suppression of D_{II}-couplings and reintroduction of D_{IS}-couplings. Furthermore, for such conditions, the magnitude of recoupled D_{IS}-coupling is very close to its global maximum.

In addition, when $\omega_{nutI}^{max} \gg \Delta\omega_{refI}^{max}$, none of the δ_{iso}^I and J_{IS} terms in $\bar{\mathscr{H}}^{(0)}$ commutes with the terms arising from D_{IS}-couplings, CSA_I, and the modulation of the carrier frequency. Therefore, if the frequencies $\omega_{D,jS}$, $\omega_{CSA,j}$, or $\Delta\omega_{refI}^{max}$ are much larger than the offset of I_j-spin, Ω_j^0, and the $2\pi J_{jS}$ coupling, the δ_{iso}^I and J_{IS} terms do not contribute to the dephasing of the I_j-spin. Subsequently when (i) $\omega_{nutI}^{max} = 3.82\omega_r \gg \Delta\omega_{refI}^{max}$ and (ii) $\sup\{\omega_{D,jS};\omega_{CSA,j};\Delta\omega_{refI}^{max}\} \gg \sup\{\Omega_j^0, 2\pi J_{jS}\}$ with $j = 1, 2$, the $\bar{\mathscr{H}}^{(0)}$ Hamiltonian of the I_2S spin system during SFAM-2 irradiation is given by

$$\bar{\mathcal{H}}^{(0)} = \sum_{j=1,2} \omega_{D,jS} I_{jZ} S_z + (\omega_{\mathrm{CSA},j} - \Delta\omega^{\max}_{\mathrm{ref}I}) I_{jZ} + 2\pi J_{II} I_1 I_2 + \Omega^0_S S_z + \bar{\mathcal{H}}^{(2)}_{\mathrm{Q},S} \qquad (14)$$

The above equation is almost identical to eq 1. The Z-axis is obtained from the B^0-axis by a rotation of $\pi/2 - \psi$ around the x-axis of the usual rotating frame (denoted $\mathcal{T}_a$ in the Supporting Information, section 1.1)

$$I_{jZ} = \sin(\psi) I_{jz} - \cos(\psi) I_{jy} \qquad (15)$$

where I_{jz} and I_{jy} are the angular moment operators in the usual rotating frame. The frequencies ω_Λ with $\Lambda = D$, jS or CSA, j in eq 14 are given by eq 3. In that case, the scaling factor κ is equal to $2J_1(\psi)/6^{1/2}$. When $\omega^{\max}_{\mathrm{nut}I} = 3.82\omega_r$, we have $\kappa = 0.47$, which is 16% larger than that of SR4^2_1. Moreover, the angle ψ is equal to 109.8° and hence the Z-axis is tilted by 19.8° from the z-direction. Equation 14 shows that the D_{IS}-coupling terms commute for different spin pairs. Therefore, these sequences do not suffer from dipolar truncation. Furthermore, the terms arising from CSA$_I$ interaction and carrier frequency modulation also commute with the D_{IS}-coupling. Therefore, the evolution of spin coherences due to D_{IS}-coupling is not affected by the CSA and the carrier frequency modulation.

In summary, eq 14 shows that SFAM-2 also achieves longitudinal two-spin-order dipolar recoupling when $\omega^{\max}_{\mathrm{nut}I} \gg \Delta\omega^{\max}_{\mathrm{ref}I}$. This condition allows employing smaller carrier frequency modulation than the regime $\omega_{\mathrm{eff}I}(t) \gg \omega_{\mathrm{app}I}(t)$, and hence reducing rf pulse transients.[59] When $\omega^{\max}_{\mathrm{nut}I} \gg \Delta\omega^{\max}_{\mathrm{ref}I}$, the rf field peak amplitude must be close to $3.82\omega_r$, in order to suppress the D_{II}-couplings. This is consistent with experiments and numerical simulations presented in ref 35. In this regime, the carrier frequency modulation only helps in averaging out the I_j-spin offsets and the J_{IS}-couplings. Therefore, the $\Delta\omega^{\max}_{\mathrm{ref}I}$ frequency must be smaller than $\omega^{\max}_{\mathrm{nut}I}$, but nonzero. Thus, the SFAM-2 recoupling under the condition $\omega^{\max}_{\mathrm{nut}I} \gg \Delta\omega^{\max}_{\mathrm{ref}I}$ and $\Delta\omega^{\max}_{\mathrm{ref}I} \neq 0$ differs from the modulatory resonance (MORE) recoupling, which consists in an amplitude-modulated irradiation at a constant carrier frequency.[60] Owing to the carrier frequency modulation, SFAM-2 displays a higher robustness to resonance offset than MORE. In practice the $\Delta\omega^{\max}_{\mathrm{ref}I}$ frequency must be larger than the maximal resonance offset. This condition ensures that the carrier frequency is swept over all the resonances during SFAM-2 irradiation. For protons, a peak amplitude of $\Delta\nu^{\max}_{\mathrm{ref}I} = \Delta\omega^{\max}_{\mathrm{ref}I}/(2\pi) \approx 15$ kHz is generally sufficient.

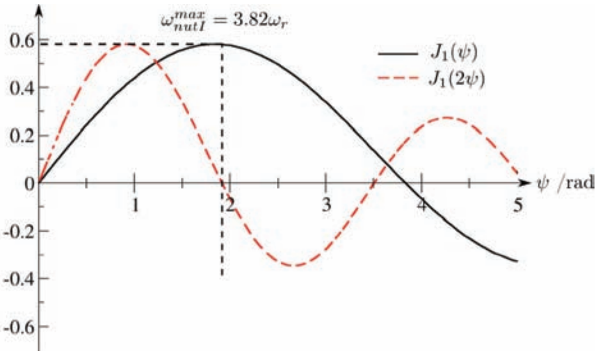

Figure 3. Plots of $J_1(\psi)$ and $J_1(2\psi)$ versus $\psi = \omega^{\max}_{\mathrm{nut}I}/(2\omega_r)$. For SFAM-2 irradiation with $\omega^{\max}_{\mathrm{nut}I} \gg \Delta\omega^{\max}_{\mathrm{ref}I}$, the magnitude of D_{IS}- and D_{II}-couplings vary with the parameter ψ, as $J_1(\psi)$ and $J_1(2\psi)$, respectively. The condition $\omega^{\max}_{\mathrm{nut}I} = 3.82\omega_r$ allows a cancelation of D_{II}-couplings, while the magnitude of D_{IS}-coupling is only 0.2% lower than the maximal value, which is obtained for $\omega^{\max}_{\mathrm{nut}I} = 3.68\omega_r$.

2.3. Efficiency versus Offset.

The SR4^2_1, SFAM-1, and SFAM-2 recoupling methods can be inserted in either channel of D-HMQC and D-HSQC experiments [see Figure 2c]. In the following, the corresponding pulse sequences are denoted D^I-HMQC and D^I-HSQC, when the heteronuclear recoupling schemes are applied to the undetected spins, and D^S-HMQC and D^S-HSQC, when the recoupling rf field is sent to the detected channel. These sequences lead to different offset dependences of the indirect observation efficiency.

2.3.1. *Recoupling Sequence Applied to the Undetected Spins.*

When the recoupling sequence is applied to the undetected spin-1/2 I nuclei, the S-spin magnetization evolves during the delays τ under the D_{IS}-couplings and the δ^S_{iso} shift, and ν^S_{QIS} shift for S-spins experiencing quadrupolar interactions.

In the D^I-HMQC experiment, the δ^S_{iso} and ν^S_{QIS} evolution during the periods τ (and t_1) is refocused by the π S-spin pulse applied in the middle of the pulse sequence. For an isolated pair of I and S nuclei, the signal intensity observed in D^I-HMQC experiment is

$$s_{D\text{-HMQC}}(\tau) \approx C\left\langle \sin^2\left(\frac{\omega_{D,IS}}{2}\tau\right)\right\rangle \qquad (16)$$

where $\langle ... \rangle$ denotes the orientational average over all possible molecular orientations in the powder and $\omega_{D,IS}$ frequency is given by eq 3 for SR4^2_1 and SFAM-2 and by eq 11 for SFAM-1. The factor C subsumes different contributions to the signal intensity, such as B^0, γ_S, the relaxation factors owing to saturation and additional losses during τ and t_1 periods, the line width, the losses arising from pulse imperfections, the receiver duty time, and the probe performances (quality factor and geometry of the coil, filling factor, lead loss).[26,61]

In the D^I-HSQC experiment, the δ^S_{iso} and possible ν^S_{QIS} evolution during the recoupling delays can be refocused in two ways: (i) either by applying two simultaneous π pulses to I- and S-spins in the middle of the fixed intervals τ, (ii) or by selecting, by the mean of phase cycling, the coherence order $p_S = +1$ during the excitation interval [see Figure 2b]. The first method is the one usually employed in J-HSQC experiments between spins 1/2 in liquids and solids.[14,16,17] In this contribution, we will focus on the second approach, denoted D^I-HSQC(+1), which allows reducing the number of pulses sent on both channels. Hence it is especially advantageous for correlation experiments involving quadrupolar nuclei, since the number of pulses sent on the quadrupolar channel is minimized. Recently, the HSQC(+1) technique was used for the indirect observation of quadrupolar nuclei with integer spin ($I = {}^{14}$N and $S = {}^1$H or ^{13}C).[8,9] The removal of the coherence pathway with $p_S = -1$ during the first τ entails a 2-fold loss of the sensitivity compared to HMQC experiment, hence

$$s_{D\text{-HSQC}(+1)}(\tau) = s_{D\text{-HMQC}}(\tau)/2 \qquad (17)$$

Finally, in the case of D^I-HSQC(±1) experiment, which allows both coherence transfer pathways during the first τ and does not comprise π pulses on both channels [see Figure 2b], the real signal intensity is equal to that of HMQC for on-resonance irradiation, but strongly depends on the offset:

$$s^{I}_{D\text{-HSQC}(\pm 1)}(\tau) \approx \mathrm{Re}\{\cos[(\Omega_S^0 + 2\pi\nu^S_{\mathrm{QIS}})\tau]\exp[\imath(\Omega_S^0 + 2\pi\nu^S_{\mathrm{QIS}})\tau]s_{D\text{-HMQC}}(\tau)\} \quad (18)$$

Equations 16−18 are valid only for an isolated *IS* pair since the homonuclear couplings among *S*-spins are not refocused during the D^I-HMQC and D^I-HSQC pulse sequences. As a result, the sensitivity of these experiments is reduced by the evolution under D_{SS} couplings during the τ intervals.

The above analytical expressions, eqs 16−18, were validated by comparison with accurate numerical simulations of the spin dynamics using realistic parameters. The simulations shown in Figure 4a used the spin system parameters defined in Table 1, which are typical for amino acids.[62] The MAS frequency and the parameters of rf and $\mathbf{B}^0$ magnetic fields are given in Table 2. All simulations were performed using Simpson software.[58] The powder averages were calculated using 2520 orientations (168 $\{\alpha_{\mathrm{MR}}, \beta_{\mathrm{MR}}\}$ pairs × 15 γ_{MR}-angles). The 168 $\{\alpha_{\mathrm{MR}}, \beta_{\mathrm{MR}}\}$ Euler angles, which relate the molecular frame to the rotor frame, were selected according to the repulsion algorithm,[63] while the γ_{MR}-angle was equally stepped from 0 to 2π rad.

In Figure 4a, the simulated indirect observation efficiency of ^{15}N−^{13}C D^I-HMQC, D^I-HSQC(+1), and D^I-HSQC(±1) schemes are plotted as a function of the carrier frequency offset, $\Delta\nu(S) = \Omega_S^0/(2\pi)$, of the detected nucleus (^{13}C). The heteronuclear dipolar couplings were recovered during τ delays by applying SFAM-1 irradiation to the undetected spin, ^{15}N. Efficiencies of indirect observation were determined by dividing the signal integral of the first row of the 2D spectrum by the integral of a signal obtained by a single $\pi/2$ *S*-pulse excitation experiment. The integrations were performed on the real part of the signal. This definition allows a direct comparison of HMQC and HSQC efficiencies. The agreement between the simulated curves and eqs 16−18 is excellent. The efficiency of D^I-HMQC is constant over the range -6 kHz $\leq \Delta\nu(S) \leq 6$ kHz and is 2 times lower than the maximal efficiency, which can be obtained in principle by optimal transfer through the J_{IS}-coupling. This loss originates from the powder average of heteronuclear dipolar coupling evolutions, since $\langle\sin^2(\omega_{D,IS}/2)\rangle \approx 0.5$ when $\tau \gg 2\pi/(\kappa b_{IS})$. Similarly, the efficiency of D^I-HSQC(+1) does not depend on the carrier frequency offset of the detected channel, but is 2 times lower than the one of D^I-HMQC, as expected from eq 17. Finally, the efficiency of D^I-HSQC(±1) varies with the detected channel offset and is perfectly fitted by the function $\cos^2[2\pi\Delta\nu(S)\tau]$, showing the validity of eq 18. Identical simulated curves were obtained when employing SFAM-2 and $\mathrm{SR4}_1^2$ sequence as the recoupling technique (simulations not shown).

2.3.2. Recoupling Sequence Applied to the Detected Spins. When the recoupling sequence is applied to the detected spin-1/2 *S* nuclei, the zero-order AHT predicts that the *S*-spin 1Q coherences evolve during the delays τ under the D_{IS}-couplings and the CSA_S. The CSA_S evolution is refocused by the π *S*-pulse in the D^S-HMQC experiment, and by the coherence pathway selection in D^S-HSQC(+1). This refocusing requires identical excitation and reconversion periods. When the CSA_S refocusing is perfect, the signal intensities observed in D^S-HMQC and D^S-HSQC(+1) experiments are given by the analytical expression of eqs 16 and 17, respectively. Thus, in the zero-order approximation, the sensitivity of *D*-HMQC and *D*-HSQC(+1) experiments does not depend on which channel is applied in the recoupling sequence.

In contrast, the sensitivity of D^S-HSQC(±1) differs from that of D^I-HSQC(±1) as the CSA_S evolution is not refocused for the *S*-spin coherence pathway −1 → 0 → −1. The signal intensity of D^S-HSQC(±1) is given by

$$s^{S}_{D\text{-HSQC}(\pm 1)}(\tau) \approx \frac{C}{2}\left\langle [1 + \exp(2\imath\omega_{\mathrm{CSA},S}\tau)]\sin^2\left(\frac{\omega_{D,IS}}{2}\tau\right)\right\rangle \quad (19)$$

In the above equation, the term $\exp(2\imath\omega_{\mathrm{CSA},S}\tau)$ originates from the *S*-spin coherence pathway −1 → 0 → −1, while the contribution from the coherence pathway +1 → 0 → −1 is independent of CSA_S. Equation 19 indicates that the signal intensity of D^S-HSQC(±1) is between those of *D*-HMQC and *D*-HSQC(+1) depending on the magnitude of the CSA_S interaction. For small CSA_S ($\gamma_S B^0 \delta^S_{\mathrm{aniso}}/(2\pi) \ll 1/\tau$), $s^S_{D\text{-HSQC}(\pm 1)}(\tau)$ must

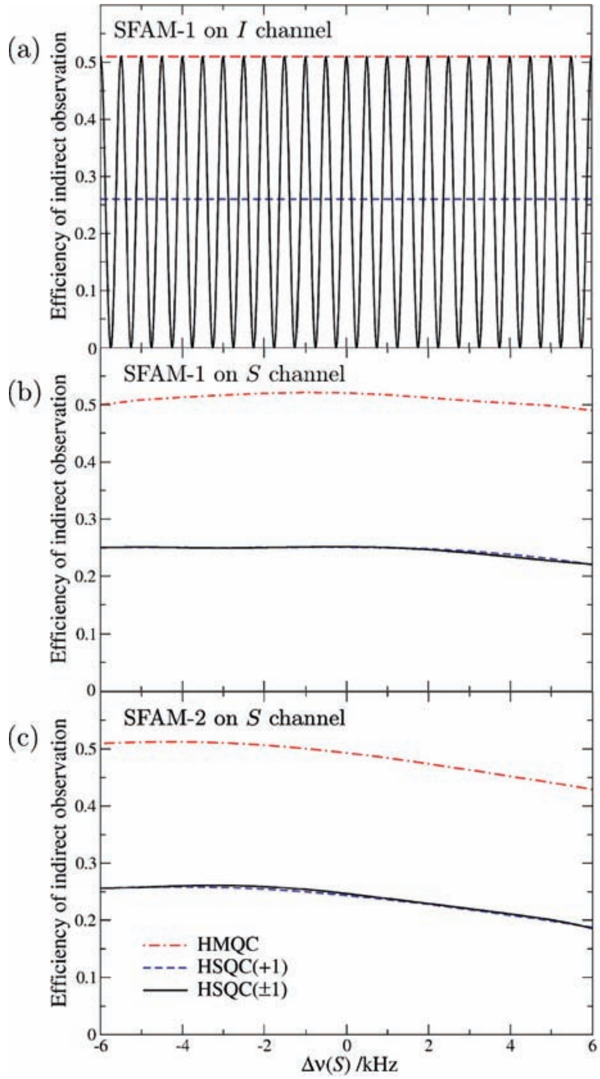

Figure 4. Numerically simulated efficiencies of indirect observation for ^{15}N−^{13}C *D*-HMQC, *D*-HSQC(±1), and *D*-HSQC(+1) sequences as function of the carrier frequency offset, $\Delta\nu(S)$, of the detected ^{13}C nucleus. The ^{15}N carrier was kept on resonance. (a) Numerical simulation for D^I-HMQC, D^I-HSQC(±1), and D^I-HSQC(+1) sequences, with SFAM-1 recoupling applied to the undetected spin, ^{15}N. (b, c) Numerical simulation for D^S-HMQC, D^S-HSQC(±1), and D^S-HSQC(+1) sequences. Two heteronuclear dipolar recoupling schemes were tested: SFAM-1 in (b) and SFAM-2 in (c). The τ intervals were fixed to 1 ms for SFAM-1 and 1.4 ms for SFAM-2, i.e., the least multiple of τ_r leading to maximal efficiency for indirect observation in each case.[34] Additional parameters used in the numerical simulations are given in Tables 1 and 2.

TABLE 1: Spin Interaction Parameters Used in the Numerical Simulations[a]

parameter	meaning	(I, S) $(^{15}N, ^{13}C)^b$	 $(^{13}C, ^1H)^c$
$(\delta^I_{\text{aniso}}, \delta^S_{\text{aniso}})$	CSA	(99 ppm, −76 ppm)	(−20 ppm, 5 ppm)
$(\eta^I_{\text{CS}}, \eta^S_{\text{CS}})$	shift tensor asymmetry parameter	(0.19, 0.90)	(0.65, 0.70)
$(\alpha^{\text{CSA},I}_{\text{PM}}, \beta^{\text{CSA},I}_{\text{PM}}, \gamma^{\text{CSA},I}_{\text{PM}})^d$	CSA_I principal axis orientation	(0, −90°, 17°)	(90°, 90°, 0)
$(\alpha^{\text{CSA},S}_{\text{PM}}, \beta^{\text{CSA},S}_{\text{PM}}, \gamma^{\text{CSA},S}_{\text{PM}})^d$	CSA_S principal axis orientation	(0, 0, 94°)	(90°, −90°, 54°)
J_{IS}	isotropic J-coupling	0 Hz	0 Hz
$b_{IS}/(2\pi)$	dipole−dipole (DD) coupling	+1 kHz	−23.3 kHz
$(\alpha^{D,IS}_{\text{PM}}, \beta^{D,IS}_{\text{PM}}, \gamma^{D,IS}_{\text{PM}})^e$	D_{IS} principal axis orientation	(0, 90°, 57°)	(0, −36°, 0)

[a] The magnitude and the orientation of the spin interaction tensors were set to typical values reported for amino acids.[62] [b] The parameters of $^{13}C-^{15}N$ spin system are realistic for $^{13}C'$ and ^{15}N nuclei of an amide group. [c] The parameters of $^{13}C-^1H$ spin system are realistic for $^{13}C^\alpha$ and $^1H^\alpha$ nuclei of an amino acid. [d] Euler angles (in degrees) relating the principal axis system of the CSA to the molecular reference frame. [e] Euler angles (in degrees) relating the principal axis system of the D_{IS} coupling between nuclei I and S to the molecular reference frame.

TABLE 2: MAS Frequency and Parameters of External Magnetic Fields Used in the Numerical Simulations

			$\nu^{\max\ d}_{\text{nut}}$ (kHz)		$\Delta\nu^{\max\ e}_{\text{ref}}$ (kHz)	
$\nu_r{}^a$ (kHz)	$\mathbf{B}^{0\ b}$ (T)	$\nu_{\text{nut}}{}^c$ (kHz)	SFAM-1	SFAM-2	SFAM-1	SFAM-2
20	9.4	150	40	56	50	20

[a] MAS frequency. [b] Static magnetic field. [c] rf nutation frequency of $\pi/2$ and π pulses. [d] Peak amplitude of rf field applied during SFAM recoupling, $\nu^{\max}_{\text{nut}} = \omega^{\max}_{\text{nut}}/(2\pi)$. [e] Peak amplitude of carrier frequency modulation for SFAM recoupling, $\Delta\nu^{\max}_{\text{ref}} = \Delta\omega^{\max}_{\text{ref}}/(2\pi)$.

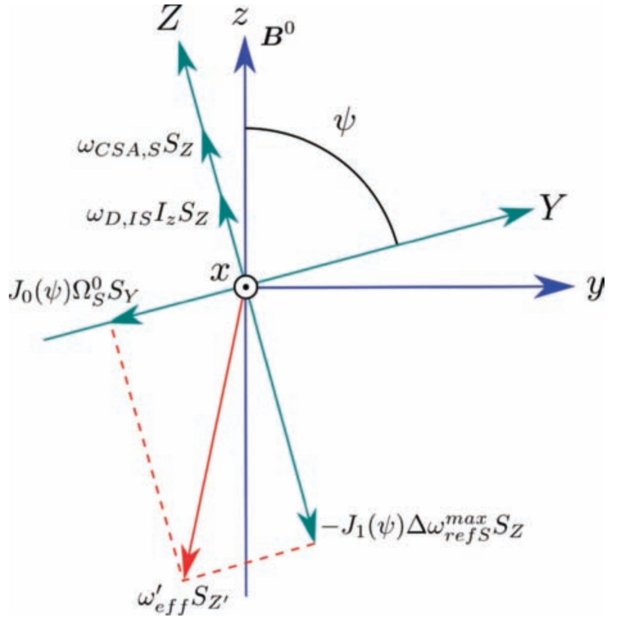

Figure 5. Schematic of the different contributions to $\bar{\mathscr{H}}^{(0)}$ for SFAM-2 irradiation on the S channel. The relative magnitudes of the interactions agree with those of the $^{13}C-^{15}N$ spin system [see Tables 1 and 2]. We assume $\omega^{\max}_{\text{nut}S} \gg \Delta\omega^{\max}_{\text{ref}S}$. The Ω^0_S offset is negative. The frequencies ω_Λ with $\Lambda = D$, IS or CSA, S are given by eq 3. The effective field, $\omega'_{\text{eff}}S_{Z'}$, is the sum of two fields: the one induced by the offset modulation, $-\Delta\omega^{\max}_{\text{ref}S}J_1(\psi)S_Z$, and the second due to the average offset, $\Omega^0_S J_0(\psi)S_Y$.

be close to the intensity of D-HMQC, while for large CSA_S the contribution from the coherence pathway $-1 \rightarrow 0 \rightarrow -1$ is averaged to zero by CSA_S defocusing and $s^S_{D\text{-HSQC}(\pm1)}(\tau) = s_{D\text{-HSQC}(+1)}(\tau) = s_{D\text{-HMQC}}(\tau)/2$. Furthermore, eq 19 shows that the sensitivity of D^S-HSQC($\pm$1) is offset-independent at zero order.

The SFAM-2 and SR4^2_1 recoupling schemes remove the homonuclear D_{SS}-coupling terms. In consequence, D^S-HMQC and D^S-HSQC pulse sequences have to be preferentially chosen when the S-spins experience strong dipolar couplings. The homonuclear J_{SS}-couplings are not suppressed. However, in most of the cases, these couplings are much smaller than the D_{IS}-couplings and, hence, have no influence on the signal intensity.

The indirect observation efficiencies of D^S-HMQC, D^S-HSQC(+1), and D^S-HSQC($\pm$1) were simulated as a function of the offset, $\Delta\nu(S)$, for two different spin systems, a $^{15}N-^{13}C$ pair and a $^{13}C-^1H$ one. Figure 4b shows the simulated efficiencies for the $^{15}N-^{13}C$ system described in Table 1, when using SFAM-1 sequence as the recoupling method. The simulation parameters are given in Table 2 and in the caption of Figure 4. They were identical to those used in Figure 4a, except that the SFAM-1 scheme was applied to the detected ^{13}C spins. In this case, the efficiency of D^S-HMQC is 0.50 for on-resonance irradiation ($\Delta\nu(S) = 0$) and hence applying the recoupling schemes to the detected spins does not lead to a loss in signal intensity. Whatever the ^{13}C offset, the efficiencies of D^S-HSQC(+1) and D^S-HSQC($\pm$1) are equal and 2 times lower than that of D^S-HMQC. This indicates that the ^{13}C CSA (10.0 kHz $\gg 1/\tau = 1.7$ kHz) is large enough to eliminate the contribution from the ^{13}C coherence pathway $-1 \rightarrow 0 \rightarrow -1$ to the detected signal. As expected from zero-order AHT [see eqs 16, 17, and 19], the three plots show little dependence on ^{13}C offset. Similar results were obtained when using SR4^2_1 as the recoupling technique (simulations not shown).

Figure 4c is analogous to Figure 4b, but SFAM-2 irradiation was employed to recouple the D_{IS}-couplings. The simulation parameters for SFAM-2 correspond approximately to the case $\omega^{\max}_{\text{nut}S} \gg \Delta\omega^{\max}_{\text{ref}S}$ [see Table 2]. Compared with Figure 4b, Figure 4c exhibits a 5% lower efficiency on resonance. This small sensitivity loss results from the +10° deviation of the Z-axis from the B^0-direction since $\psi = 80°$ [see eqs 14 and 15]. The asymmetrical dependence of the efficiency with $\Delta\nu(S)$ agrees with the tilt of the effective field. As seen in Figure 5 and shown in the Supporting Information, section 1.3, the effective field is the sum of the carrier frequency modulation term, $-\Delta\nu^{\max}_{\text{ref}S}J_1(\psi)S_Z$, and the isotropic chemical shift term, $\Delta\nu(S)$ $J_0(\psi)S_Y$, where $J_0(\psi)$ is the zero-order Bessel function of the first kind. Consequently, there is a negative offset value $\Delta\nu(S)$ such that

$$\arccos(\Delta\nu^{\max}_{\text{ref}S}J_1(\psi)/\{[\Delta\nu^{\max}_{\text{ref}S}J_1(\psi)]^2 + [\Delta\nu(S)\ J_0(\psi)]^2\}^{1/2}) = 10° \quad (20)$$

i.e., $\Delta\nu(S) = -3.4$ kHz, where the effective field points in the ($-B^0$)-direction. This condition yields maximal efficiency, as seen in Figure 4c.

Figure 6 illustrates the case where CSA_S is small. The spin system was the $^{13}C-^1H$ pair described in Table 1. In Figure

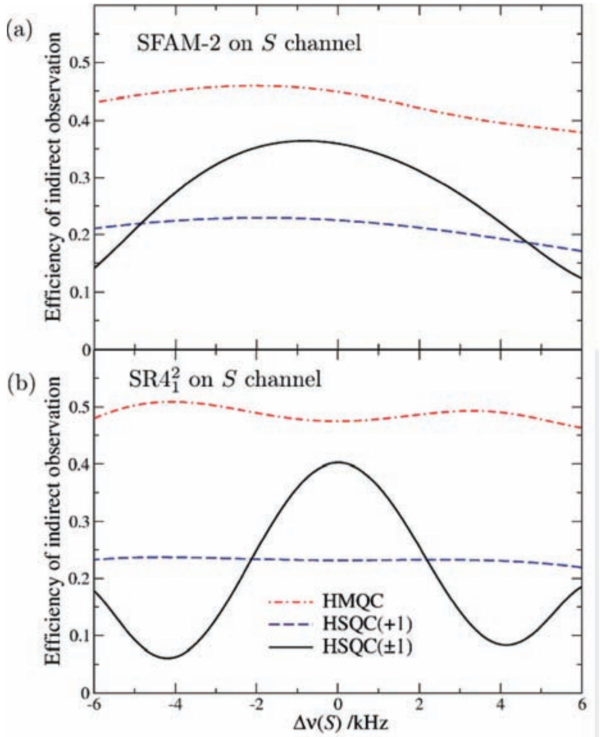

Figure 6. Numerically simulated efficiencies of indirect observation for ^{13}C−^{1}H D^S-HMQC, D^S-HSQC(±1), and D^S-HSQC(+1) sequences as function of the carrier frequency offset, $\Delta\nu(S)$, of the detected ^{1}H nucleus. The ^{13}C $\pi/2$ pulses were applied on resonance. Two different heteronuclear dipolar recoupling schemes were tested: SFAM-2 (a) and SR4_1^2 (b). The τ intervals were fixed to 0.3 ms. Additional parameters used in the numerical simulations are given in Tables 1 and 2.

6a, SFAM-2 was employed as the recoupling method. The simulation parameters are given in Table 2. They were identical to those employed in Figure 4c, but a shorter recoupling time was used because of the larger b_{IS} constant. The comparison of Figures 4c and 6a shows that the simulated efficiencies of D^S-HMQC and D^S-HSQC(+1) for the ^{13}C−^{1}H pair are similar to those obtained for a ^{15}N−^{13}C system. In contrast, the on-resonance efficiency of D^S-HSQC(±1) is higher when ^{1}H nuclei are detected instead of ^{13}C. This efficiency (0.35) is between those of D^S-HSQC(+1) (0.23) and D^S-HMQC (0.46), because the 1Q proton coherences are only partially defocused during τ periods by the small ^{1}H CSA (2 kHz ≈ $1/\tau = 3$ kHz). Nevertheless, the signal intensity of D^S-HSQC(±1) varies with the offset. This modulation originates from nonzero-order terms in the AH, which depends on $\Delta\nu(S)$.

Figure 6b shows the results of numerical simulations when using SR4_1^2. The recoupling sequences apart, the simulation parameters were the same as those of Figure 6a. The relative efficiencies of D^S-HMQC, D^S-HSQC(+1), and D^S-HSQC(±1) including SR4_1^2 recoupling are globally similar to those obtained for SFAM-2 [see Figure 6a]. However, the offset dependence of the signal intensity differs between SR4_1^2 and SFAM-2. In particular, the SR4_1^2 recoupling leads to a stronger offset dependence of D^S-HSQC(±1) efficiency than SFAM-2. This phenomenon must be related to the different cycle times between SFAM-2 and SR4_1^2. Indeed, the isotropic chemical shift terms in $\bar{\mathcal{H}}^{(0)}$ are averaged to zero over one rotor period in the case of SFAM-2, whereas they are only suppressed by the phase inversion supercycle extending over two τ_r in the case of SR4_1^2. Furthermore, the SFAM-2 sequence benefits from a better robustness to rf inhomogeneity than the SR4_1^2 method.[35]

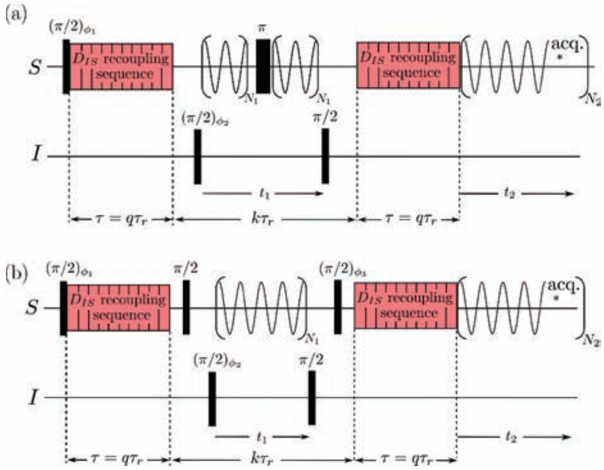

Figure 7. Pulse sequences for (a) D^S-HMQC and (b) D^S-HSQC experiments with C8_1^4(half-cos) and wC8_1^4(half-cos) irradiations applied during t_1 and t_2 evolution periods, respectively. The phase cyclings were identical to those given in the caption of Figure 2. Homonuclear dipolar recoupling sequences were applied on the detected channel.

2.4. Homonuclear Dipolar Decoupling. The HMQC and HSQC pulse sequences can be applied to observe lower γ nuclei, such as ^{13}C or ^{14}N, through nearby high-γ isotopes, such as ^{1}H.[5,6,14,16] Proton is an ideal spy nucleus because of its high gyromagnetic ratio and its high isotopic natural abundance. However, this combination generally entails strong homonuclear couplings among the protons. These homogeneous anisotropic interactions[64] are not completely averaged out by the MAS, and hence, the ^{1}H−^{1}H strong dipolar couplings can reduce the sensitivity of HMQC and HSQC experiments as well as the spectral resolution in both direct (F_2) and indirect (F_1) dimensions. In the case of indirect detection via the protons ($S = {}^{1}$H), the line broadening in F_1 dimension originates from the noncommutation of Hamiltonians representing D_{SS}- and D_{IS}-couplings.

As explained in subsection 2.3.2, the SS dipolar coupling evolution during the τ delays can be suppressed by applying recoupling sequences, such as SR4_1^2 or SFAM-2, to the spy spins. The enhancement of resolution in F_1 and F_2 dimensions requires the use of windowless and windowed homonuclear decoupling sequences in the t_1 and t_2 periods, respectively. So far various decoupling techniques, including frequency switched Lee−Goldberg (FSLG)[17,18,65−67] and DUMBO,[68,69] were used in HSQC and HMQC experiments. However, they were not applied to the detected spin. In this article, we explore the use of C$N_n^{N/2}$ irradiation on the detected channel during t_1 and t_2 times.[10,50,51] A half-cosine pulse was used as the basic C element and the corresponding pulse sequences are denoted C$N_n^{N/2}$(half-cos) in the following. These symmetry-based schemes have the benefit of creating a broad-banded z-rotation of nuclear spins, thus allowing the elimination of zero and image peaks, without the requirement of preparatory pulses. Furthermore, the scaling factor is offset-independent and conventional phase cycling can be employed in multidimensional experiments. Finally these new CRAMPS sequences require lower rf power than PMLG and DUMBO, partly because their rf amplitude can be modulated.[51,70] Applying C$N_n^{N/2}$ schemes to the S-spins suppresses, in the zero-order AH, D_{SS}- and D_{IS}-couplings as well as CSA$_S$, but preserves δ_{iso}^S chemical shift, J_{IS}-couplings, and J_{SS}-couplings.[51]

Windowless C$N_n^{N/2}$ sequences can be implemented straightforwardly in the indirect dimension of the HSQC variant, devoid of a π S-pulse during t_1 [see Figure 7b], while windowed C$N_n^{N/2}$ decoupling (denoted wC$N_n^{N/2}$ in the following) is required during the acquisition period, t_2.[49] In contrast, only a subgroup of $CN_n^{N/2}$ sequences can be inserted during the t_1 period of HMQC because of the presence of a π S-pulse in the middle of t_1 time [see Figure 7a]. We found that $CN_1^{N/2}$ symmetries, where N is a multiple of 8, can incorporate a short π pulse in their middle, while keeping their decoupling properties. These symmetries are also suitable for HSQC experiments, which employs a π S-pulse during t_1 to refocus the J_{IS}-couplings.[14,16,17]

3. Experimental Demonstrations

3.1. Samples and Experimental Conditions. All the experiments were performed on a wide-bore Bruker AVANCE II 400 MHz NMR spectrometer operating at a magnetic field of 9.4 T, using samples of isotopically substituted α-(2-^{13}C,^{15}N)-glycine,[71] isotopically unmodified L-histidine·HCl, and monosodium dihydrogenophosphate (NaH_2PO_4). The amino acids and NaH_2PO_4 were purchased from Sigma-Aldrich and Prolabo, respectively, and were used without purification. The samples were confined to the middle of the rotor in order to improve the B_1 homogeneity.

The ^{1}H and ^{13}C chemical shifts are referenced to tetramethylsilane (TMS). The ^{23}Na chemical shifts are referenced to a 1 mol·L^{-1} NaCl aqueous solution.[72] For 2D spectra recorded with homonuclear dipolar decoupling [see Figures 9d,e and 10c], the frequency scales of F_2 projections were divided by the experimentally determined scaling factors to restore the actual chemical shift values.

The glycine sample was spun at 20 kHz in a wide-bore triple-resonance 3.2 mm MAS NMR probe. The 1D ^{15}N−^{13}C D-HMQC, D-HSQC(±1), and D-HSQC(+1) spectra with ^{13}C detection [see Figure 8] were obtained with 64 scans and a recycle delay of 1.5 s. The interval between the two $(\pi/2)^I$ pulses, t_1 [see Figure 2], was fixed to τ_r. A rotor-synchronized gap of 100 μs ($k = 2$ in Figure 2) separated the two recoupling intervals. Cross-polarization (CP) transfer from protons to carbons (with $\nu_{1,CP}(^1H) = 75$ kHz, $\nu_{1,CP}(^{13}C) = 55$ kHz, and $\tau_{CP} = 1$ ms) replaced the first $(\pi/2)^S$ pulse in the sequences of Figure 2. During the remaining part of the sequences, a SPINAL-64 decoupling sequence with $\nu_{1,dec}(^1H) = 105$ kHz was applied to the ^{1}H channel. The rf nutation frequencies of the hard pulses were 105 kHz for ^{1}H, 77 kHz for ^{13}C, and 56 kHz for ^{15}N. SFAM-2 recoupling schemes were applied during $\tau = 22\tau_r = 1.1$ ms on either the ^{13}C or ^{15}N channels. In both cases, the peak values of the rf nutation frequency and the maximum offsets were $\nu_{nut}^{max} = 40$ kHz and $\Delta\nu_{ref}^{max} = 25$ kHz, respectively.

The L-histidine·HCl and NaH_2PO_4 samples were spun at 31.746 kHz in a wide-bore triple-resonance 2.5 mm MAS probe. The 2D X−^{1}H through-space correlation spectra were recorded by using D^S-HMQC and D^S-HSQC sequences. $SR4_1^2$ recoupling with a rf nutation frequency of 63.5 kHz was applied to the ^{1}H channel. A rotor-synchronized gap of $k\tau_r$ ($k = t_1/\tau_r + 2$ in Figures 2 and 7) separated the two recoupling intervals. The peak value of the rf nutation frequency for $C8_1^4$(half -cos) and $wC8_1^4$(half-cos) irradiations was 130 kHz.

The 2D ^{13}C−^{1}H D^S-HMQC and D^S-HSQC spectra of L-histidine·HCl with ^{1}H detection [see Figure 9] result from averaging 64 transients for each of 350 t_1 increments with $\Delta t_1 = \tau_r = 31.5$ μs and a recycle delay of 1.5 s. The τ delays were equal to $6\tau_r = 189$ μs. The rf nutation frequencies of the hard pulses were 67 kHz for ^{1}H and 71 kHz for ^{13}C.

The 2D ^{23}Na−^{1}H D^S-HMQC spectra of NaH_2PO_4 with ^{1}H detection [see Figure 10] result from averaging 320 transients for each of 120 t_1 increments with $\Delta t_1 = \tau_r = 31.5$ μs and a recycle delay of 1.5 s. As the ^{1}H T_1 relaxation time of NaH_2PO_4 is 23 s, two rf pulses of 16 ms with orthogonal phases were applied at the beginning of the pulse sequence on the ^{1}H channel in order to ensure equivalent conditions for each transient. The rf nutation frequency of this pulse pair satisfies the rotary resonance recoupling (R^3) condition $\nu_{nut}^H = \nu_r$,[27,28,44] which reintroduces D_{HH} and D_{NaH} couplings as well as CSA_H under MAS condition. Thus these R^3 pulses eliminate any residual ^{1}H coherences remaining after the t_2 period. The τ delays were equal to $\tau = 12\tau_r = 378$ μs. The rf field strengths of ^{1}H hard pulses and ^{23}Na central transition selective pulses were 67 and 9 kHz, respectively.

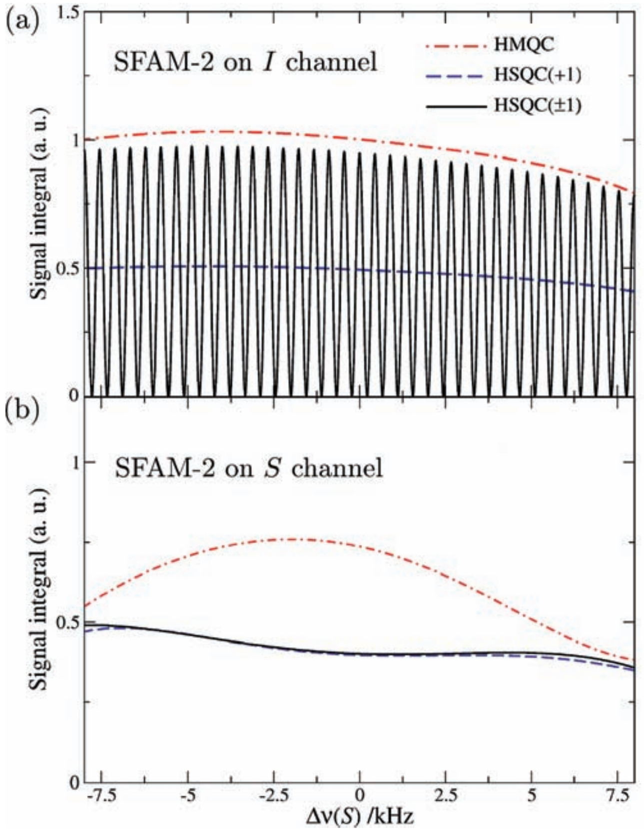

Figure 8. Experimental signal integrals of (2-^{13}C,^{15}N)-glycine measured for 1D ^{15}N−^{13}C D-HMQC, D-HSQC(+1), and D-HSQC(±1) experiments as function of the carrier frequency offset, $\Delta\nu(S)$, of the detected ^{13}C nucleus. The employed pulse sequences are depicted in Figure 2. During τ intervals, heteronuclear dipolar recoupling schemes, SFAM-2, were applied either (a) to the undetected channel, ^{15}N, or (b) to the detected one, ^{13}C. Signal integrals were normalized to the on-resonance signal integral of D^I-HMQC experiment. Additional details are given in the experimental section.

3.2. Efficiency versus Offset. To evaluate the validity of eqs 16−19, the dependence of D-HMQC and D-HSQC signal intensity with the offset of the detected spin was measured experimentally. To that end, several 1D ^{15}N−^{13}C D-HMQC, D-HSQC(+1), and D-HSQC(±1) experiments were performed on (2-^{13}C,^{15}N)-glycine. The heteronuclear recoupling sequences, SFAM-2, were applied either to the undetected spin, $I = {}^{15}$N, or to the detected one, $S = {}^{13}$C.

Figure 8a shows the experimental dependence of signal integral with ^{13}C offset, when ^{15}N nuclei are subjected to SFAM-2 irradiation. The D^I-HMQC experiment yields the highest indirect observation efficiency, whereas the sensitivity of D^I-HSQC(+1) is 2 times lower. The efficiency of these sequences weakly depends on the ^{13}C offset, whereas the D^I-HSQC(±1) signal integral oscillates with $\Delta\nu(S)$ between zero and that of D^I-HMQC.

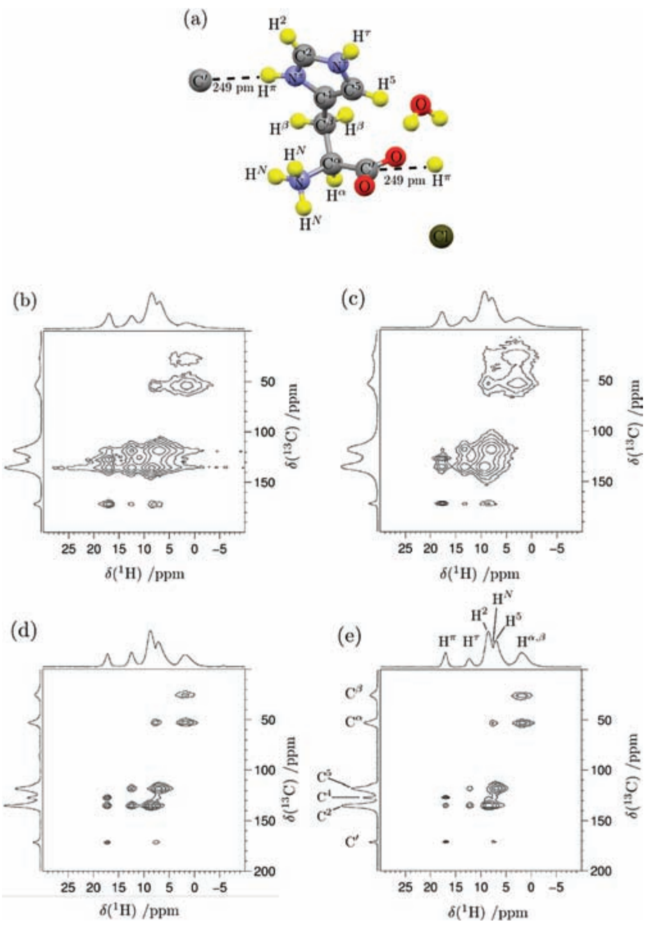

Figure 9. (a) Structure of L-histidine·HCl obtained from neutron diffraction[75] with IUPAC atom labeling.[76] (b−e) Experimental 2D ^{13}C−^{1}H D^S-HMQC (b, d) and D^S-HSQC(±1) (c, e) spectra of isotopically unmodified L-histidine·HCl at $\nu_r = 31.746$ kHz. Spectra b and c were recorded by employing the pulse sequences of Figure 2, whereas spectra d and e were obtained by using the schemes of Figure 7, which include C8_1^4(half-cos) and wC8_1^4(half-cos) irradiations during t_1 and t_2 periods. ^{13}C−^{1}H dipolar couplings were restored by applying SR4_1^2 recoupling to the detected ^{1}H channel. Additional details are given in the experimental section.

These experimental variations of indirect observation efficiency with $\Delta\nu(S)$ are quite similar to those predicted from eqs 16−18, or calculated by numerical simulations [see Figure 4a]. This confirms the validity of the theoretical analysis presented in section 2. The main difference with simulations lies in the weak experimental dependence of D^I-HMQC and D^I-HSQC(+1) efficiencies with $\Delta\nu(S)$. First, this dependence may originate from finite rf power. Second, the variation in ^{13}C offset affects the efficiency of the initial ^{1}H−^{13}C CP transfer, which replaces the first ^{13}C $\pi/2$ pulse.

The insertion of SFAM-2 sequence in the detected channel $S = {}^{13}$C yields different experimental dependences of signal integral with ^{13}C offset, as seen in Figure 8b. The efficiencies of D^S-HSQC(+1) and D^S-HSQC(±1) experiments are almost equal over the range $\Delta\nu(S) = \pm\ 8$ kHz. Furthermore, on resonance, the sensitivity of D^S-HSQC experiments is 2 times lower than that of D^S-HMQC. These observations agree with simulations shown in Figure 4c and indicate that the CSA of glycine α-carbon atom ($\delta_{\text{aniso}}^{C^{\alpha}} = -19.4$ ppm)[73,74] is large enough to suppress the contribution from the ^{13}C coherence pathway $-1 \rightarrow 0 \rightarrow -1$ to D^S-HSQC(±1) signal intensity. Compared to the simulations, the experimental efficiency of D^S-HMQC exhibits a stronger dependence with ^{13}C offset. The slight offset dependence owing to the tilt of the Z-axis is enhanced by changes in the efficiency of the initial ^{1}H−^{13}C CP transfer and imperfect refocusing of ^{13}C CSA by the middle π pulse for a large resonance offset.

The comparison of Figure 8a and 8b evidences that, in the case of weak dipolar couplings among the detected spins, it is preferable to apply the heteronuclear recoupling sequences to the undetected nuclei and to employ D^I-HMQC.

3.3. ^{13}C−^{1}H *D*-HMQC and *D*-HSQC 2D Spectra.

The *D*-HMQC and *D*-HSQC experiments were also compared in the case of indirect detection via the protons. Figure 9 shows the 2D ^{13}C−^{1}H D^S-HMQC and D^S-HSQC(±1) spectra of isotopically unmodified L-histidine·HCl. The 2D ^{13}C−^{1}H D^S-HSQC(+1) spectra are not shown since the intensities of correlation peaks in this spectra are lower than those of 2D D^S-HSQC(±1) spectra [see Figure 9c,e]. The SR4_1^2 sequences were applied to the detected channel $S = {}^{1}$H in order to suppress the D_{HH} dephasing during the τ delays. Applying the SR4_1^2 scheme to the undetected channel $I = {}^{13}$C prevents the observation of correlation peaks, C$^{\alpha}$−H$^{\alpha}$ and C$^{\beta}$−H$^{\beta}$, between aliphatic carbon-13 and proton nuclei.

Figure 9b,c shows the 2D ^{13}C−^{1}H D^S-HMQC and D^S-HSQC(±1) spectra recorded without homonuclear decoupling, while Figure 9d,e displays the 2D D^S-HMQC and D^S-HSQC(±1) spectra obtained when applying C8_1^4(half-cos) and wC8_1^4(half-cos) homonuclear decoupling during t_1 and t_2 periods, respectively. The comparison of Figure 9b and 9d, and 9c and 9e, clearly evidences that C8_1^4 homonuclear decoupling sequences allow improving the spectral resolution in both F_1 and F_2 dimensions. In particular, the C^4 signal is resolved in the F_1 projections of Figure 9d,e, whereas it is hardly visible in the projections of Figure 9b,c. More quantitatively, the use of C8_1^4(half-cos) decoupling yields a 3-fold decrease in line width of the C$^{\alpha}$ peak, while the scaled-up line width of the H$^{\alpha}$ peak is divided by a factor of 2 when employing wC8_1^4(half-cos) irradiation during the t_2 period.

The assignment of the 1D ^{13}C and ^{1}H spectra has been previously reported.[71,77] In the 2D spectra of Figure 9, all the protonated carbons are correlated with their attached protons ($d_{\text{CH}} = 103-110$ pm and $-28.0\ \text{kHz} \le b_{\text{CH}} \le -23.0$ kHz). For the chosen excitation and reconversion periods, $\tau = 189$ μs, intramolecular two-bond cross-peaks are also observed but they are less intense than the one-bond correlations. The two-bond cross-peaks result from ^{1}H−^{13}C contacts at $d_{\text{CH}} = 207-223$ pm ($-3.4\ \text{kHz} \le b_{\text{CH}} \le -2.7$ kHz). Longer range cross-peaks include the intramolecular three-bond correlation, C′−H^{N}, and the intermolecular correlation, C′−H$^{\pi}$ ($d_{\text{C'H}^{\pi}} = 249$ pm and $b_{\text{C'H}^{\pi}} = -1.9$ kHz).

The relative intensities of D^S-HSQC(±1) and D^S-HMQC cross-peaks, $s^S_{D\text{-HSQC}(\pm1)}/s^S_{D\text{-HMQC}}$, fluctuate between 0.5 and 1 depending on the ^{1}H sites, whereas the intensities of D^S-HSQC(+1) cross-peaks are 2 times lower than those of D^S-HMQC. These results are consistent with the low CSA of protons in organic compounds[78] and the numerical simulations of Figure 6. The fluctuation of $s^S_{D\text{-HSQC}(\pm1)}/s^S_{D\text{-HMQC}}$ between the different protons ensues from the dependence of $s^S_{D\text{-HSQC}(\pm1)}$ with proton CSA and offset, $\Delta\nu(S)$. Anyway, the D^S-HMQC experiment yields the highest signal-to-noise ratio. Furthermore, in this case, no significant differences in the F_1 spectral resolution were observed between D^S-HMQC and D^S-HSQC experiments. In conclusion, the D^S-HMQC experiment outperforms D^S-HSQC(±1) and D^S-HSQC(+1) techniques in this case.

3.4. ^{23}Na−^{1}H *D*-HMQC and *D*-HSQC 2D Spectra.

Finally, the *D*-HMQC and *D*-HSQC experiments were employed for

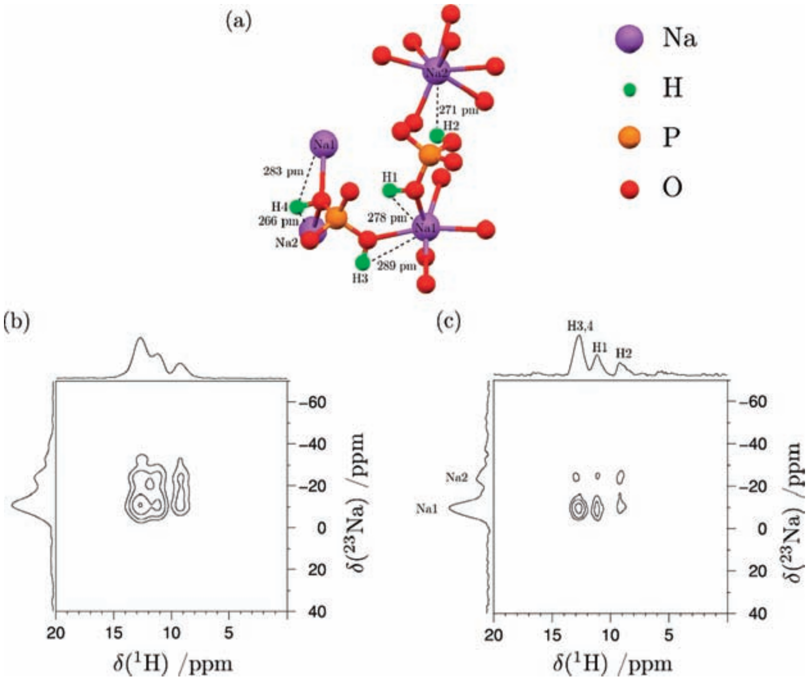

Figure 10. (a) Atomic structure of NaH_2PO_4. The H−Na distances shorter than 2.9 Å are displayed as dashed lines. (b, c) Experimental 2D $^{23}Na-^{1}H$ D^S-HMQC spectra of NaH_2PO_4 at $\nu_r = 31.746$ kHz. Spectrum b was recorded by employing the pulse sequences of Figure 2a, whereas spectrum c was obtained from the scheme displayed Figure 7a; i.e., $C8_1^4$(half-cos) and $wC8_1^4$(half-cos) irradiations were applied during t_1 and t_2 periods, respectively. $^{23}Na-^{1}H$ dipolar couplings were restored by applying $SR4_1^2$ recoupling to the detected ^1H channel. Additional details are given in the experimental section.

the indirect detection of half-integer quadrupolar nuclei, $I = {}^{23}Na$, via the protons, $S = {}^{1}H$. The D_{HH} dephasing during the τ delays was removed by applying the $SR4_1^2$ sequences to the protons. The 2D $^{23}Na-^{1}H$ D^S-HMQC and D^S-HSQC experiments were performed on a model inorganic compound, NaH_2PO_4.

Figure 10c shows the D^S-HMQC spectrum recorded with $^1H-^1H$ decoupling [see Figure 7]. This 2D spectrum correlates through D_{NaH}-couplings the $\delta_{iso}(^1H)$ shifts in the F_2 dimension with the chemical and quadrupolar isotropic shifts of ^{23}Na nuclei in the F_1 dimension. For comparison, the same spectrum recorded without homonuclear decoupling is shown in Figure 10b. The use of $C8_1^4$(half-cos) and $wC8_1^4$(half-cos) sequences improves the spectral resolution in both F_1 and F_2 dimensions, as evidenced by the comparison of the 2D spectrum projections. In particular, the H3,4 and H1 signals are better resolved in Figure 10c than in Figure 10b.

NaH_2PO_4 unit cell contains four nonequivalent protons (denoted H1 to H4) and two distinct sodium sites (Na1 and Na2). The assignment of $\delta_{iso}(^1H)$ shifts has been already reported and is given in Table 3 as well as in Figure 10c.[79] The differences in δ_{iso} between the proton sites result from disparity in hydrogen bond lengths between the phosphate groups.[80−82] The 1D ^{23}Na MAS NMR spectrum consists of two overlapping second-order quadrupolar line shapes. The NMR parameters resulting from deconvolution of the ^{23}Na line shapes are given in Table 4.

The assignment of the ^{23}Na spectrum was derived from the 2D D^S-HMQC spectrum in Figure 10c. We used the fact that the intensity of correlation peaks in D^S-HMQC experiment depends on the size of the effective heteronuclear couplings, and hence on the $^{23}Na-^{1}H$ distance. First, the H2 site exhibits in Figure 10c a much weaker correlation peak with the deshielded ^{23}Na resonance than the other protons. Second, the neutron diffraction structure[83] reveals that the H2 proton is much closer to the Na2 site than to the Na1 site, since the closest Na2−H2 and Na1−H2 distances are 271 and 368 pm, respectively ($b_{Na2H2} = -1.6$ kHz and $b_{Na1H2} = -0.6$ kHz). Third, the other protons are much closer to the Na1 atom than the H2 site is ($d_{Na1H1} = 278$ pm, $d_{Na1H3} = 289$ pm, and $d_{Na1H4} = 283$ pm).

TABLE 3: Experimental and Calculated ^1H NMR Parameters of NaH_2PO_4

		experimental	calculated[b]		
site	d_{OO}[a] (pm)	δ_{iso}[c] (ppm)	δ_{iso}[d] (ppm)	δ_{aniso}[e] (ppm)	η_{CS}[e]
H1	257	11.1	11.2	22.7	0.11
H2	263	9.3	9.3	20.2	0.08
H3	255	12.4	12.4	23.4	0.12
H4	249	12.8	12.9	24.6	0.10

[a] The O···H−O distances, d_{OO}, were estimated from the DFT-optimized structure. [b] The calculated parameters result from the DFT-GIPAW calculations on the DFT-optimized structure. [c] The ^1H chemical shifts are referenced to tetramethylsilane (TMS). [d] The calculated chemical shifts are shifted by a constant value to match the calculated value for H2 with the most experimental shielded resonance. [e] The definitions of δ_{aniso} and η_{CS} are given below eq 5.

TABLE 4: Experimental and Calculated ^{23}Na NMR Parameters of NaH_2PO_4

site	method[a]	δ_{iso}[b] (ppm)	C_Q (kHz)	η_Q
Na1	exp	−2.5	1.6	0.5
	calc	−2.5	1.46	0.46
Na2	exp	−6.4	2.4	0.9
	calc	−5.95	1.95	0.88

[a] The experimental (exp) parameters are obtained by fitting the 1D ^{23}Na MAS NMR spectrum with dmfit program,[97] while the calculated (calc) parameters result from the DFT-GIPAW calculations on the DFT-optimized structure. [b] The ^{23}Na chemical shifts are referenced to a 1 mol·L^{-1} NaCl aqueous solution.[72] The calculated chemical shifts are shifted by a constant value to match the calculated value for Na1 with the most experimental deshielded resonance.

Subsequently, the deshielded and shielded ^{23}Na resonances must stem from Na1 and Na2 nuclei, respectively.

This assignment was corroborated by periodic density functional theory (DFT) calculations, using the Quantum-ESPRESSO code.[84,85] We used the PBE functional for the generalized gradient approximation (GGA) of the exchange-correlation functional.[86] The wave function is expanded on a plane-wave basis set with an energy cutoff of 100 Ry. The potentials due to the ions were represented by norm-conserving Troullier−Martins pseudopotentials.[87] The electronic configurations involved in the construction of the pseudopotentials for the different nuclei Na, P, O, and H are $\{2s^2\ 2p^6\ 3d^0\}$, $\{3s^2\ 3p^3\ 3d^0\}$, $\{2s^2\ 2p^{3.5}\ 3d^0\}$, and $\{1s^{0.1}\}$ with respective core radii (in atomic units) {1.81 1.25 1.8}, {1.63 1.8 1.93}, {1.43 1.43 1.43}, and {1.2}. The electronic structure gives access to the electric field gradient (EFG) tensor through the reconstruction of the all-electron wave function obtained with the projector augmented wave (PAW) approach.[88,89] The parameters describing the quadrupolar interaction, C_Q and η_Q, are related to the principal components (V_{xx},V_{yy},V_{zz}) of the EFG tensor by $C_Q = eQ|V_{zz}|/h$ and $\eta_Q = (V_{xx} - V_{yy})/V_{zz}$, where by convention $|V_{xx}| \le |V_{yy}| \le |V_{zz}|$, Q is the nuclear quadrupole moment, h is the Planck constant, and e is the elementary charge.[55] In the present work, we used $Q = 10.4$ fm^2 for ^{23}Na nuclei.[90] As the sign of C_Q is, in most cases, not determined directly from a simple MAS spectrum, absolute values of C_Q have been considered. The calculation of the absolute chemical shielding was performed using GIPAW algorithms developed by Pickard and Mauri.[91] The calculation of NMR parameters requires the accurate knowledge of the structure. Hence the NMR parameters were determined after DFT optimization of the neutron-diffraction structure.[83] We used the VASP code[92,93] for the structure optimization, with GGA-PW91 functional[94] and the PAW scheme[95] to describe the electron−ion interactions and an energy cutoff of 44 Ry for the expansion of the plane-wave basis set.

The calculated ^{1}H δ_{iso}, δ_{aniso}, and η_{CS} values are reported in Table 3. There is a remarkable agreement between the calculated and experimental δ_{iso} differences, while the calculated δ_{aniso} and η_{CS} are consistent with those reported in the literature for P−O···H−O−P hydrogen bonds.[96] The ^{1}H CSA decreases with increasing O···H−O distances.[80−82] The large magnitude of ^{1}H CSA in NaH_2PO_4 is confirmed by the 2-fold lower efficiency of D^S-HSQC(±1) and D^S-HSQC(+1) experiments [not shown] compared to that of D^S-HMQC. These relative experimental efficiencies agree with the numerical simulations of Figure 4c corresponding to the case of large CSA$_S$ of the detected spins. Therefore, the comparison of on-resonance sensitivities between D^S-HSQC(±1), D^S-HSQC(+1), and D^S-HMQC experiments yields a qualitative assessment of CSA$_S$.

^{23}Na NMR parameters resulting from the DFT-GIPAW calculations are given in Table 4. The comparison between the experimental and calculated NMR parameters confirms the assignment of ^{23}Na resonance based on a 2D D^S-HMQC spectrum. Indeed, the isotropic chemical shift of Na2 is computed 3.5 ppm lower than the one of Na1, in excellent agreement with the experimentally observed difference (3.9 ppm). Furthermore, the calculated and experimental η_Q values are close. The η_Q value of Na1 nucleus is smaller than that of Na2, since the primary coordination sphere of the octahedral site Na1 is more symmetrical than that of the Na2 site, which is surrounded by seven oxygen atoms. The relative magnitude of calculated C_Q values is also consistent with the experimental ones, although the agreement between the computed values and the experimental ones is less good: the computed C_Q values are clearly underestimated. Nevertheless, assignment is unambiguous and confirms the attribution resulting from *D*-HMQC and *D*-HSQC experiments.

4. Conclusion

We have compared the performances of different *D*-HMQC and *D*-HSQC variants. These experiments allow obtaining 2D heteronuclear correlation spectra by using dipolar couplings to transfer the coherences between unlike spins. These sequences do not suffer from dipolar truncation and enable the indirect detection of low-γ isotopes via high-γ nuclei. The indirectly detected spins and the spy nucleus can be either spin-1/2 or quadrupolar nuclei. For correlation between spin-1/2 and quadrupolar nuclei, the heteronuclear recoupling is achieved by irradiating only the spin-1/2 isotope. This prevents any interference between quadrupolar interaction and rf irradiation.

We have shown that the efficiency and the robustness to resonance offset depend on the sequence design as well as on the magnitude of spin interactions. The investigated *D*-HMQC and *D*-HSQC versions differ by the heteronuclear recoupling methods (SR4_1^2, SFAM-1, and SFAM-2), the channel in which this recoupling is inserted (detected or undetected), and, for HSQC sequences, the selected coherence pathways during the excitation time.

When the dipolar interactions between the *S*-spins are weak enough to be averaged out by MAS, the D^I-HMQC version offers the largest efficiency over a broad $\Delta\nu(S)$ range. Furthermore, the SFAM-1 technique must be employed since it requires a shorter recoupling time than SFAM-2 and SR4_1^2, owing to its larger scaling factor.[35] This allows minimizing the irreversible losses of signal during excitation and reconversion delays.

When the dipolar interactions between the *S*-spins are not averaged out solely by MAS, SFAM-2, or SR4_1^2 recoupling methods must be applied to the *S*-spins. SFAM-2 sequence requires slightly higher rf power than SR4_1^2, but it has the benefit of decreasing rf pulse transients and is more robust to rf homogeneity. This is advantageous, especially under ultrafast MAS ($\nu_r = 65-70$ kHz). Furthermore, for large D_{SS}-couplings, we have shown that the D^S-HMQC experiment is more sensitive than the D^S-HSQC techniques. In principle, the HSQC scheme can provide an advantage in terms of resolution in the indirect dimension.[8,9,68] However, in the investigated examples, no significant gain was observed when using HSQC. We have demonstrated that the resolution in both spectral dimensions can be enhanced by using windowless and windowed C8_1^4(half-cos) homonuclear decoupling in the t_1 and t_2 periods, respectively.

For NaH_2PO_4 compound, the 2D ^{23}Na−^{1}H D^S-HMQC experiment incorporating C8_1^4(half-cos) decoupling has enabled the assignment of ^{23}Na spectrum from the ^{1}H isotropic chemical shifts. We have circumvented the long ^{1}H relaxation times in such a compound, by using a pair of R^3 pulses at the beginning of the sequence. The resonance assignment was corroborated by periodic DFT calculations of the ^{23}Na and ^{1}H chemical shift tensors and the ^{23}Na quadrupolar coupling tensor.

The D^S-HMQC and D^S-HSQC spectra reported in this paper were carried out on model samples, but these techniques are applicable to a wide variety of crystalline and amorphous compounds. They are expected to become very useful in the structural investigation of solids containing quadrupolar nuclei. When the amount of *I* nuclei is low (observation of isotopes with low natural abundance in diluted or surface species), dedicated techniques must be employed in order to eliminate the "t_1-noise"[61] contributed by *S* nuclei that do not participate in polarization transfer to *I* nuclei.[26,28,29,31,98]

The theoretical aspects of this work extend previous treatments of SFAM sequences by deriving analytical expressions for SFAM-2 irradiation under conditions closer to those used experimentally. In particular, we have demonstrated that SFAM-2 sequence allows the reintroduction of heteronuclear dipolar couplings, even if the carrier frequency modulation is small. Under this condition, the peak amplitude of the rf field must be close to $3.82\omega_r$ in order to suppress the homonuclear dipolar couplings. Furthermore, this theoretical treatment underlines the relationships between SFAM methods and symmetry-based pulse sequences. Hence, the implementation of amplitude and carrier frequency modulations for various symmetry-based sequences may be envisaged.

Acknowledgment. The authors are grateful for funding provided by Region Nord/Pas de Calais, Europe (FEDER), CNRS, French Minister of Science, FR-3050, USTL, ENSCL, Bruker BIOSPIN, and ANR Contract No. NT05-2-41632. We acknowledge the Bruker company and Fabien Aussenac for the lending of a wide-bore 2.5 mm Bruker MAS NMR probe. F.D. thanks the National Natural Science Foundation of China (20773159 and 20673139) and the National Basic Research Program of China (2009CB918600) for financial support.

Supporting Information Available: Derivation of the average Hamiltonian expressions for SFAM sequence. This material is available free of charge via the Internet at http://pubs.acs.org.

References and Notes

(1) Fyfe, C. A.; Grondey, H.; Mueller, K. T.; Wong-Moon, K. C.; Markus, T. *J. Am. Chem. Soc.* **1992**, *114*, 5876–5878.

(2) Fyfe, C. A.; zu Altenschildesche, H. M.; Wong-Moon, K. C.; Grondey, H.; Chezeau, J. M. *Solid State Nucl. Magn. Reson.* **1997**, *9*, 97–106, In Honour of Gunter Engelhardt.

(3) Cavadini, S.; Lupulescu, A.; Antonijevic, S.; Bodenhausen, G. *J. Am. Chem. Soc.* **2006**, *128*, 7706–7707.

(4) Gan, Z. *J. Am. Chem. Soc.* **2006**, *128*, 6040–6041.

(5) Gan, Z. *J. Magn. Reson.* **2007**, *184*, 39–43.

(6) Gan, Z.; Amoureux, J. P.; Trébosc, J. *Chem. Phys. Lett.* **2007**, *435*, 163–169.

(7) Cavadini, S.; Abraham, A.; Bodenhausen, G. *Chem. Phys. Lett.* **2007**, *445*, 1–5.

(8) Cavadini, S.; Abraham, A.; Bodenhausen, G. *J. Magn. Reson.* **2008**, *190*, 160–164.

(9) Antonijevic, S.; Halpern-Manners, N. *Solid State Nucl. Magn. Reson.* **2008**, *33*, 82–87.

(10) Amoureux, J.-P.; Hu, B.; Trébosc, J. *J. Magn. Reson.* **2008**, *193*, 305–307.

(11) Amoureux, J.-P.; Trébosc, J.; Delevoye, L.; Lafon, O.; Hu, B.; Wang, Q. *Solid State Nucl. Magn. Reson.* **2009**, *35*, 12–18.

(12) Burum, D. P.; Ernst, R. R. *J. Magn. Reson.* **1980**, *39*, 163–168.

(13) Morris, G. A. *J. Am. Chem. Soc.* **1980**, *102*, 428–429.

(14) Maudsley, A. A.; Ernst, R. R. *Chem. Phys. Lett.* **1977**, *50*, 368–372.

(15) Müller, L. *J. Am. Chem. Soc.* **1979**, *101*, 4481–4484.

(16) Bodenhausen, G.; Ruben, D. J. *Chem. Phys. Lett.* **1980**, *69*, 185–189.

(17) Lesage, A.; Emsley, L. *J. Magn. Reson.* **2001**, *148*, 449–454.

(18) Lesage, A.; Sakellariou, D.; Steuernagel, S.; Emsley, L. *J. Am. Chem. Soc.* **1998**, *120*, 13194–13201.

(19) Massiot, D.; Fayon, F.; Alonso, B.; Trébosc, J.; Amoureux, J.-P. *J. Magn. Reson.* **2003**, *164*, 160–164.

(20) Stejskal, E. O.; Schaefer, J.; Waugh, J. S. *J. Magn. Reson.* **1977**, *28*, 105–112.

(21) Caravatti, P.; Bodenhausen, G.; Ernst, R. *Chem. Phys. Lett.* **1982**, *89*, 363–367.

(22) Hing, A. W.; Vega, S.; Schaefer, J. *J. Magn. Reson.* **1992**, *96*, 205–209.

(23) Trébosc, J.; Hu, B.; Amoureux, J.; Gan, Z. *J. Magn. Reson.* **2007**, *186*, 220–227.

(24) Gullion, T.; Schaefer, J. *J. Magn. Reson.* **1989**, *81*, 196–200.

(25) Gullion, T.; Vega, A. J. *Prog. Nucl. Magn. Reson. Spectrosc.* **2005**, *47*, 123–136.

(26) Ishii, Y.; Tycko, R. *J. Magn. Reson.* **2000**, *142*, 199–204.

(27) Ishii, Y.; Yesinowski, J. P.; Tycko, R. *J. Am. Chem. Soc.* **2001**, *123*, 2921–2922.

(28) Wiench, J. W.; Bronnimann, C. E.; Lin, V. S.-Y.; Pruski, M. *J. Am. Chem. Soc.* **2007**, *129*, 12076–12077.

(29) Zhou, D. H.; Shah, G.; Comos, M.; Mullen, C.; Sandoz, D.; Rienstra, C. M. *J. Am. Chem. Soc.* **2007**, *129*, 11791–11801.

(30) Zhou, D. H.; Rienstra, C. M. *Angew. Chem., Int. Ed.* **2008**, *47*, 7328–7331.

(31) Mao, K.; Wiench, J. W.; Lin, V. S.-Y.; Pruski, M. *J. Magn. Reson.* **2009**, *196*, 92–95.

(32) Brinkmann, A.; Levitt, M. H. *J. Chem. Phys.* **2001**, *115*, 357–384.

(33) Hong, M.; Griffin, R. G. *J. Am. Chem. Soc.* **1998**, *120*, 7113–7114.

(34) Saalwächter, K.; Spiess, H. W. *J. Chem. Phys.* **2001**, *114*, 5707.

(35) Hu, B.; Trébosc, J.; Amoureux, J. *J. Magn. Reson.* **2008**, *192*, 112–122.

(36) Baldus, M.; Meier, B. H. *J. Magn. Reson.* **1997**, *128*, 172–193.

(37) Hodgkinson, P.; Emsley, L. *J. Magn. Reson.* **1999**, *139*, 46–59.

(38) Vega, A. J. *J. Magn. Reson.* **1992**, *96*, 50–68.

(39) Hu, B.; Amoureux, J.; Trébosc, J.; Hafner, S. *J. Magn. Reson.* **2008**, *192*, 8–16.

(40) Amoureux, J.-P.; Pruski, M. *Mol. Phys.* **2002**, *100*, 1595–1613.

(41) Brinkmann, A.; Kentgens, A. *J. Phys. Chem. B* **2006**, *110*, 16089–16101.

(42) Levitt, M. H. In *Encyclopedia of Nuclear Magnetic Resonance*; Wiley: Chichester, 2002.

(43) Levitt, M. H.; Oas, T. G.; Griffin, R. G. *Isr. J. Chem.* **1988**, *28*, 271.

(44) Oas, T. G.; Griffin, R. G.; Levitt, M. H. *J. Chem. Phys.* **1988**, *89*, 692.

(45) Gan, Z.; Grant, D. M. *Chem. Phys. Lett.* **1990**, *168*, 304–308.

(46) Gan, Z.; Grant, D. M.; Ernst, R. R. *Chem. Phys. Lett.* **1996**, *254*, 349–357.

(47) Fu, R.; Smith, S. A.; Bodenhausen, G. *Chem. Phys. Lett.* **1997**, *272*, 361–369.

(48) Nishimura, K.; Fu, R.; Cross, T. A. *J. Magn. Reson.* **2001**, *152*, 227–233.

(49) Brinkmann, A.; Kentgens, A. *J. Am. Chem. Soc.* **2006**, *128*, 14758–14759.

(50) Amoureux, J.-P.; Hu, B.; Trébosc, J.; Wang, Q.; Lafon, O.; Deng, F. *Solid State Nucl. Magn. Reson.* **2009**, *35* (1), 19–24.

(51) Lafon, O.; Wang, Q.; Hu, B.; Trébosc, J.; Deng, F.; Amoureux, J.-P. *J. Chem. Phys.* **2009**, *130*, 014504.

(52) Haeberlen, U.; Waugh, J. S. *Phys. Rev.* **1968**, *175*, 453–467.

(53) Haeberlen, U. *High-Resolution NMR in Solids: Selective Averaging*; Academic: New York, 1976.

(54) Mauri, F.; Pfrommer, B. G.; Louie, S. G. *Phys. Rev. Lett.* **1996**, *77*, 5300–5303.

(55) Jerschow, A. *Prog. Nucl. Magn. Reson. Spectrosc.* **2005**, *46*, 63–78.

(56) Marion, D.; Ikura, M.; Tschudin, R.; Bax, A. *J. Magn. Reson.* **1989**, *85*, 393–399.

(57) Nielsen, N. C.; Bildsøe, H.; Jakobsen, H. J.; Levitt, M. H. *J. Chem. Phys.* **1994**, *101*, 1805–1812.

(58) Bak, M.; Rasmussen, J. T.; Nielsen, N. C. *J. Magn. Reson.* **2000**, *147*, 296–330.

(59) Vega, A. J. *J. Magn. Reson.* **2004**, *170*, 22–41.

(60) Takegoshi, K.; Takeda, K.; Terao, T. *Chem. Phys. Lett.* **1996**, *260*, 331–335.

(61) Ernst, R. R.; Bodenhausen, G.; Wokaun, A. *Principles of nuclear magnetic resonance in one and two dimensions*; Oxford University Press: Oxford, 1987.

(62) Bak, M.; Schultz, R.; Vosegaard, T.; Nielsen, N. C. *J. Magn. Reson.* **2002**, *154*, 28–45.

(63) Bak, M.; Nielsen, N. C. *J. Magn. Reson.* **1997**, *125*, 132.

(64) Maricq, M. M.; Waugh, J. S. *J. Chem. Phys.* **1979**, *70*, 3300–3316.

(65) Bielecki, A.; Kolbert, A. C.; Levitt, M. H. *Chem. Phys. Lett.* **1989**, *155*, 341–346.

(66) Bielecki, A.; Kolbert, A. C.; Levitt, M. H. *Adv. Magn. Reson.* **1989**, *14*, 111.

(67) Levitt, M. H.; Kolbert, A. C.; Bielecki, A.; Ruben, D. J. *Solid State Nucl. Magn. Reson.* **1993**, *2*, 151–163.

(68) Lesage, A.; Sakellariou, D.; Hediger, S.; Elena, B.; Charmont, P.; Steuernagel, S.; Emsley, L. *J. Magn. Reson.* **2003**, *163*, 105–113.

(69) Sakellariou, D.; Lesage, A.; Hodgkinson, P.; Emsley, L. *Chem. Phys. Lett.* **2000**, *319*, 253–260.

(70) Mafra, L.; Coelho, C.; Siegel, R.; Rocha, J. *J. Magn. Reson.* **2009**, *197*, 20–27.

(71) Kimura, H.; Nakamura, K.; Eguchi, A.; Sugisawa, H.; Deguchi, K.; Ebisawa, K.; Suzuki, E.; Shoji, A. *J. Mol. Struct.* **1998**, *447*, 247–255.

(72) Hayashi, S.; Hayamizu, K. *Bull. Chem. Soc. Jpn.* **1989**, *62*, 2429–2430.

(73) Brinkmann, A.; Schmedt auf der Günne, J.; Levitt, M. H. *J. Magn. Reson.* **2002**, *156*, 79–96.

(74) Haberkorn, R. A.; Stark, R. E.; Van Willigen, H.; Griffin, R. G. *J. Am. Chem. Soc.* **1981**, *103*, 2534–2539.

(75) Fuess, H.; Hohlwein, D.; Mason, S. A. *Acta Crystallogr., Sect. B: Struct. Sci.* **1977**, *33*, 654–659.

(76) IUPAC-IUB Joint Commission on Biochemical Nomenclature. *Pure Appl. Chem.* **1984**, *56*, 595−624.

(77) Madhu, P.; Vinogradov, E.; Vega, S. *Chem. Phys. Lett.* **2004**, *394*, 423–428.

(78) Brouwer, D. H.; Ripmeester, J. A. *J. Magn. Reson.* **2007**, *185*, 173–178.

(79) Mafra, L.; Gomes, J. R. B.; Trébosc, J.; Rocha, J.; Amoureux, J.-P. *J. Magn. Reson.* **2009**, *196*, 88–91.

(80) Ditchfield, R. *J. Chem. Phys.* **1976**, *65*, 3123–3133.

(81) Berglund, B.; Vaughan, R. W. *J. Chem. Phys.* **1980**, *73*, 2037–2043.

(82) Rohlfing, C. M.; Allen, L. C.; Ditchfield, R. *J. Chem. Phys.* **1983**, *79*, 4958–4966.

(83) Choudhary, R. N. P.; Nelmes, R. J.; Rouse, K. D. *Chem. Phys. Lett.* **1981**, *78*, 102–105.

(84) Kohn, W.; Sham, L. J. *Phys. Rev.* **1965**, *140*, 1133.

(85) See http://www.quantum-espresso.org.

(86) Perdew, J. P.; Burke, K.; Ernzerhof, M. *Phys. Rev. Lett.* **1996**, *77*, 3865–3868.

(87) Troullier, N.; Martins, J. L. *Phys. Rev. B* **1991**, *43*, 1993–2006.

(88) Blöchl, P. E. *Phys. Rev. B* **1994**, *50*, 17953–17979.

(89) Profeta, M.; Mauri, F.; Pickard, C. J. *J. Am. Chem. Soc.* **2003**, *125*, 541–548.

(90) Pyykkö, P. *Mol. Phys.* **2008**, *106*, 1965–1974.

(91) Pickard, C. J.; Mauri, F. *Phys. Rev. B* **2001**, *63*, 245101.

(92) Kresse, G.; Furthmüller, J. *Phys. Rev. B* **1996**, *54*, 11169–11186.

(93) Kresse, G.; Hafner, J. *Phys. Rev. B* **1993**, *48*, 13115–13118.

(94) Perdew, J. P.; Burke, K.; Wang, Y. *Phys. Rev. B* **1996**, *54*, 16533–16539.

(95) Kresse, G.; Joubert, D. *Phys. Rev. B* **1999**, *59*, 1758–1775.

(96) Duma, L.; Abergel, D.; Tekely, P.; Bodenhausen, G. *Chem. Commun.* **2008**, 2361–2363.

(97) Massiot, D.; Fayon, F.; Capron, M.; King, I.; Le Calvé, S.; Alonso, B.; Durand, J.-O.; Bujoli, B.; Gan, Z.; Hoatson, G. *Magn. Reson. Chem.* **2002**, *40*, 70–76.

(98) Zhou, D. H.; Rienstra, C. M. *J. Magn. Reson.* **2008**, *192*, 167–172.

JP906099K